heritage

MDPI

Article

Portable X-ray Fluorescence (p-XRF) Uncertainty Estimation for Glazed Ceramic Analysis: Case of Iznik Tiles

Belgin Demirsar Arli [1], Gulsu Simsek Franci [2,*], Sennur Kaya [3], Hakan Arli [4] and Philippe Colomban [5,*]

1 Department of Art History, Faculty of Letters, Istanbul University, Balabanaga Mah. Ordu Cad. 6, Laleli, Fatih, 34134 Istanbul, Turkey; beldemar@istanbul.edu.tr
2 KUYTAM (Surface Science and Technology Center), College of Sciences, Rumelifeneri Campus, Koç University, Rumelifeneri Yolu, Sariyer, 34450 Istanbul, Turkey
3 Department of Fine Arts, Istanbul University, Balabanaga Mah. Vezneciler Cad. 11, Laleli, Fatih, 34134 Istanbul, Turkey; kayasen@istanbul.edu.tr
4 Directorate of Iznik Tile Kilns Excavation, Yeşil Camii Mah. Kilicarslan Cad. No: 196, Iznik, 16860 Bursa, Turkey; arlihkn@gmail.com
5 MONARIS UMR8233, Sorbonne Université, CNRS, 4 Place Jussieu, 75005 Paris, France
* Correspondence: gusimsek@ku.edu.tr (G.S.F.); philippe.colomban@sorbonne-universite.fr or philippe.colomban@upmc.fr (P.C.)

Received: 14 October 2020; Accepted: 7 November 2020; Published: 10 November 2020

Abstract: The aim of this study is to estimate the uncertainty of a portable X-ray fluorescence (p-XRF) instrument for the (semi-quantitative) analyses of tiles with underglaze decoration. Before starting the campaign of on-site measurements, the optimum acquisition time and the most accurate calibration mode were selected. For this purpose, the elemental composition of two glass standards of NIST (SRM610 and SRM612) and a Corning A standard were measured with varied times (5–360 s) and in different calibration modes (Mining, Mining Light Elements, Soil, and Rare Earth Elements). Afterwards, a set of blue-and-white tiles that was unearthed at Iznik Tile Kilns Excavation between the dig seasons of 2015 and 2019 was examined with p-XRF by selecting ten points of measure from each layer (body, transparent glaze, and blue coloured areas). The elemental composition of different layers was evaluated by means of the intragroup and intergroup data. They were also compared to the previous studies and found that the corrosion-free, homogeneous, and non-porous surfaces decrease the relative standard deviation (RSD) by increasing the consistency of the compositional data. The major elements found in the matrix of each layer (Al and Si for the body, Pb and Sn for the glaze) have the lowest value of RSD, as expected. However, the comparison of the data with the analysis of the reference materials showed that the content of Mg and also Si, which belong to the low-Z elements group, is shifted relatively towards the higher compositional values. The impossibility of measuring the elemental composition of sodium does not hinder the classification of the samples. Although the transition metals have very low concentrations, p-XRF measurements appear rather consistent and the intrinsic scattering of the data observed for a single artefact is largely smaller than those observed for the tiles of different historical buildings. Thus, it allows the classification to be made related to the different techniques used.

Keywords: p-XRF; penetration depth; glaze; body; cobalt; bismuth; manganese; tin; nickel; error

1. Introduction

The use of portable instruments, particularly p-XRF, with the improvement of their performances and the reduction of their price profoundly modifies the practices in archaeometry [1–15]. However,

the potential for the misuse of the instrument has resulted in scepticism towards the technique and its application in the area of archaeological materials due to the several perceived weaknesses of the portable/handheld system [16–22]. The first weakness of portable XRFs is the variability of their positioning due to constraints on-site and the complex shape of many objects. A second intrinsic weakness is that the volume analysed will be very different related to the element measured, hence the penetration depth of the light elements (Mg, Al, Si, K, and Ca) is close to the surface and is over several hundreds of μm for heavier elements like lead (Pb) and gold (Au) and several mm for tin (Sn), antimony (Sb),and so on [23]. However, the absorption of X-rays by air prohibits the measurement of very light elements (B, C, O, and Na). The measurements of low-Z elements are therefore very sensitive to possible corrosion, often evidenced in the metallic objects but also glasses, specifically excavated ones. Re-normalization procedures in comparison with the similar uncorroded references may be applied [24]. The "wrong" choice of the calibration mode during the analyses with p-XRF also unfavorably affects the results, which remain subject to discussion. Different calibration methods will be introduced in detail in the section on the XRF procedures.

An evaluation of the measurement "error" for the different types of materials is therefore essential to establish that differences observed are significant and to discuss their technical and historical implications. Variations related to the object's heterogeneity also induce measurement shift, which complicates classification by comparison of the elemental composition.

Several studies have been carried out on the comparison of p-XRF measurements with lab-scale, high-resolution instruments (wavelength dispersive XRF (WD-XRF), laser ablation inductively coupled plasma-mass spectrometry (LA-ICP-MS), atomic emission spectrometry (ICP-AES), and'neutron activation analysis (NAA)). The results were interpreted by plotting correlations, slopes, and multivariate statistics diagrams in comparison with the elements measured and/or techniques used [2,3,25–27]. Most of these studies cover the characterization of homogeneous, matrix-consistent materials, for example, ancient glasses and high temperature fired ceramics. The latter studies, in which the number of the elements (5–10) was limited, represent mostly the elemental composition of high-Z elements (Nb, Zr, Sr, etc.) [2,3,26]. The studies demonstrated that a non-destructive p-XRF instrument has analytical consistency with ICP-AES, ICP-OES (inductively coupled plasma-optical emission spectrometry), and NAA techniques in distinguishing different production groups of cultural materials. It should be noted that these high-tech instruments require an additional step, namely the calibration process before the measurement of the samples, e.g., preparation of the calibration curve for each ICP analysis [28], involving regular measurements of STG standards with WD-XRF after each maintenance of the instrument [29]. An external calibration procedure may also apply for the ceramic analyses with p-XRF by using reference glass samples (Corning, Brill, NIST SRM 610, 612) [24] and geological standards (red mud and diorite DR-N) [30]. For instance, in the study of Liu et al. [3], a Corning glass D whose composition was determined by ICP-AES was used to estimate the reliability of the p-XRF instrument, before starting the measurements of potash glass beads. The error data found in these articles will be used to compare with our results.

The previous studies of our group cover a wide range of elements due to the complex microstructure of the historical artefacts. The glazed ceramics that we examine with p-XRF usually contain four different layers of variable thickness including the transparent glaze, layers which contain the colouring agents, slip (if present) layer, and body substrate [31–34]. A previous study was carried out to compare and reveal the reliability of both techniques, WD-XRF and p-XRF, by analyzing a set of Chinese blue-and-white porcelains [29]. The results were favourably given as the mean values of each measurement carried out on the body, glaze, and coloured areas, to limit some of the probable analysis errors. A comparison of the elemental ratios has been generally preferred for the interpretation of the compositional data [33]. To go deeper into establishing a reliable procedure for the p-XRF analysis, we selected four representative blue-and-white glazed tiles unearthed from ancient Iznik tile kilns [32]. Firstly, we developed a pXRF methodology to apply for the analysis of glazed ceramics by performing test measurements of the reference glasses (NIST SRM610, SRM612, and Corning A), and consecutively,

we measured ten points from each layer of the selected tiles. Each single "studied spot" (shown in Appendix A, Figures A1–A4) is added in the scatter plots of the examined layers, i.e., body, transparent glaze, and blue décor, to show the compositional variations. The objective is to measure and compare the standard deviation factor of the major, minor, and trace elements as a function of the ceramic and geometry parameters (glaze thickness, heterogeneity of the glaze/body, etc.) and then to estimate an error bar that will be applied for the determination of the characteristic parameters of Iznik productions (Al_2O_3/SiO_2, PbO/SiO_2, Sn/Pb, CoO/MnO/NiO ratio, etc.) analyzed on-site.

Iznik pottery artefacts, which are considered the most sophisticated ceramic productions of the Ottoman era [35–38] equivalent to the magnificent Chinese [39], Japanese [40], and European porcelains [41], have always attracted intensive attention from research scholars and connoisseurs since the 19th century [42–49]. They aimed to discover the production technology of these unique masterpieces. The panels of tiles that were produced in Iznik kilns usually decorate the wall revetments of historical buildings [50–54], and some of them (e.g., Selimiye Mosque in Edirne and holy places in Bursa) are conserved as world heritage sites by UNESCO. The complex structure of Iznik ceramics, which arises from the presence of multilayers (body, slip, multicoloured underglaze decors, and transparent glaze), serves to control the efficiency of portable analytical instruments, i.e., p-XRF in our case. Moreover, understanding the production technology will allow us to question the connection between the ancient Anatolian ceramic centres (Byzantine, Seljuks) and the external ones (Samarqand, Chinese). Therefore, the study of the tiles, which are the local productions of Iznik kilns, is crucial.

2. Experimental

2.1. Artefacts

Hundreds of mono and polychrome decorated and/or glazed sherds, which were unearthed during the excavation seasons from 2015 to 2019 at the Iznik Tile Kilns Excavation site [32], were examined with a handheld XRF (hh-XRF) instrument (Figure 1) to identify the composition of the body, glaze, and colouring agents (blue, green, turquoise, red decors, and black lines) for the purpose of classification. The measurements were carried out by contacting the instrument gently on the glazed and bodied (unglazed) sides of the sherds, as was done on site in the historical buildings (Figure 1) [33]. Before the compositional analyses, a macroscopic examination of the cross-sections was carried out with a stereo microscope to measure the thickness of the glaze for estimating the penetration depth of the elements measured. Three of them (see Figure 1 centre, which represent "blue-and-white" productions, and one being a Rhodes work were chosen to reveal any potential uncertainties of the instrument for the analysis of glazed ceramics. IZN/15 (from the 2015 excavation season) and IZN/17 (2017 season) are decorated with a similar lightness of the blue colour, in addition to the turquoise-coloured areas. The blue colour of the sherd, IZN/16 (2016 season), is darker than the others, and the tone of the white area is milky rather than a yellowish hue, which is observed particularly in the glaze of IZN/19. IZN/16 is dated to the 16th century, while IZN/15, IZN/17, and IZN/19 are accepted by social scientists (art historians and archaeologists) to be produced in the 17th century [50–54]. The blue colour in IZN/19 is encountered under the yellowish-green glaze. The glossy surface of IZN/16, which is well-preserved, proves the absence of any corrosion of the glaze. Conversely, the glaze of the other three sherds, especially that of IZN/19, is matte and rough. The loss of gloss in the glaze may arise from the surface corrosion (leaching of potassium ions, protonation, or crack formation) and/or an incomplete firing of the pieces. Excavated sherds are rubbish materials from fabrication. Distribution of the glaze thickness for a series of Iznik tiles is given in Appendix A, Figure A5.

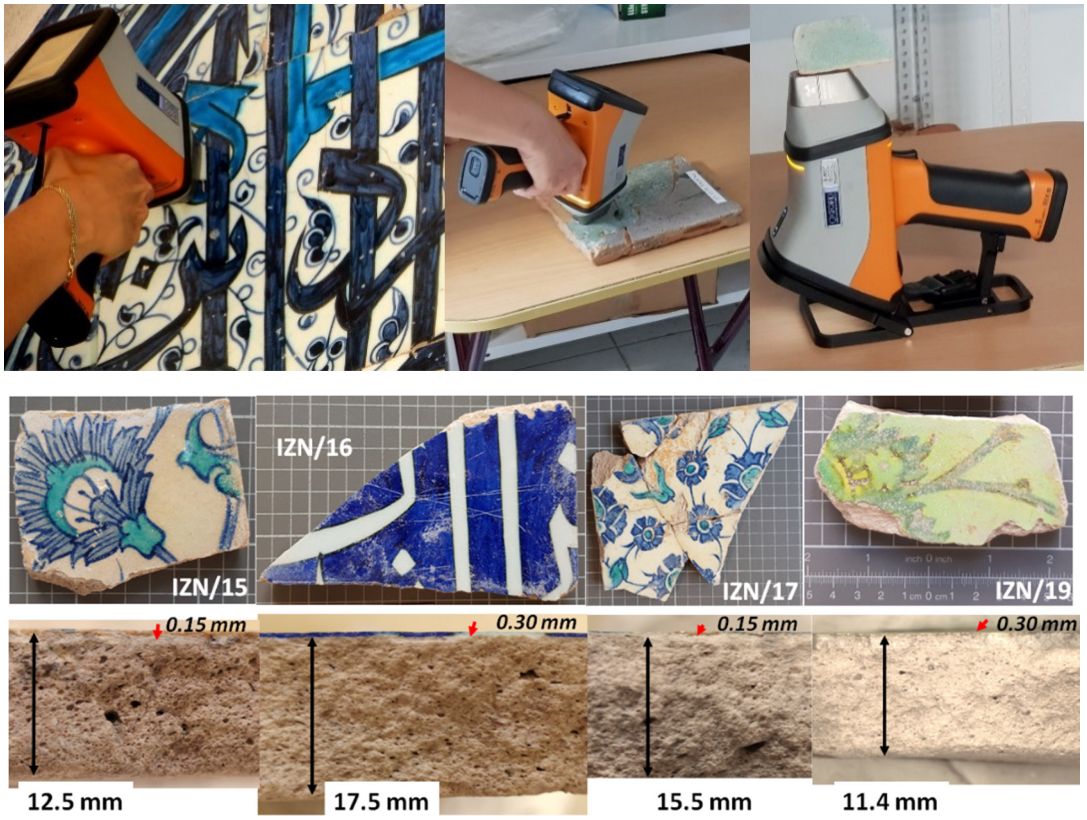

Figure 1. Examples of on-site use of hh-XRF instrument: (**top-left**) on-site measurement of the tile panel of Üç Şerefeli Mosque in Edirne, and (**centre**) and (**top-right**) measurements at the Iznik Tile Kilns Excavation' house; (**bottom**), representative images of the sherds of tiles. IZN/15, IZN/16, and IZN/17 belong to the group of "blue-and-white" tiles, while IZN/19 is known as a Rhodes work. Cross-sections (from Bilge Çubukçu) show the thicknesses of the glaze and paste.

2.2. XRF Procedure

XRF analysis was performed using a handheld Hitachi X-MET 8000 Expert Geo (Oxford Instruments) system equipped with rhodium (Rh) target X-ray tube of 4 W, 50 kV max, and a silicon drift detector (SDD). Later generation p-XRF spectrometers contain built-in calibrations installed in the operating software of the instrument at the factory before reaching the end-user [27,29]. Different methods are created according to the different materials to be measured. Soil mode, which measures the high-Z elements preferentially (from K and onwards in the periodic table), is used for the analysis of sediments. The Rare Earth Elements (REE) mode, which additionally measures La, Ce, Pr, Nd, and Hf, is usually applied for the measurement of obsidians, which contain trace elements in their composition. Mining (Mg, Al, Si, P, and S excluded) and Mining Light Elements (Mg, Al, Si, P, S, and Cl included) modes are chosen for the measurements of glass, pottery, and glazed ceramics. Additionally, the Alloy mode is included for the metals/alloys' analyses. Before our group started the campaign of studies of Iznik tiles with p-XRF [32–34], four calibration methods (Soil, Mining, Mining Light Elements, Rare Earth Elements) were tested on the analyses of the reference glass standards (NIST SRM610, SRM612, and Corning A), and the most accurate mode was found to be Mining Light Elements, which was also determined in the previous study [29]. This method operates in the measurement at double excitation energies, whereas the first one uses the low energy at 8 keV for determining the elemental composition of the low Z elements (Mg, Si, Al, P, S, Cl), and the second one uses a high energy at 45 keV to identify the network modifiers (K, Ca, Pb) and blue colouring agents (Mn, Fe, Co, Ni, Cu, Bi) found in the decor. The beam size at the surface was around 1 cm^2, and a camera was used to control the measurement points, which were selected from ten different areas (shown in Appendix A,

Figures A1–A4) representing the composition of the body, "white" glaze, and blue coloured area with the aim of identifying the variation.

The acquisition time was determined after a group of sequential analyses of the glass standards by measuring them at different periods of time. We measured three standards (the elemental compositions are listed in Appendix A, Table A1) at 5, 10, 15, 20, 30, 60, 120, 180, and 360 s. The shorter acquisition time allowed us to better determine the composition of the low-Z elements, but there was not enough time to detect the heavier elements (e.g., Pb, Sn, etc.). Indeed, the longer acquisition time is more reliable than the shorter radiation time, but the use of the instrument manually does not allow one to hold it steady throughout 180 or 360 s. Unfortunately, this p-XRF instrument may not be attached to a tripod due to its configuration. The results of the elemental analyses also showed that the optimum acquisition time was 30 s for the determination of both low and high-Z elements. Moreover, the variation of the data determined at different acquisition times is rather narrow, and this confirms the consistency of the instrument. The results obtained from the standard materials were also compared to the data already published in the literature [55,56]. Figure 2a shows the scatter plots of Al_2O_3 versus SiO_2, where a slight shift towards higher concentration values is observed by comparison with the nominal composition for the measurement of the glass standards with our p-XRF instrument. Note that the measured data are distributed isotopically. On the contrary, the determination of the minor and trace elements in the blue coloured areas was found to be more accurate at shorter acquisition times. Figure 2b shows the distribution of the radiation periods applied on the measurements of glass standards compared to the literature data. The elemental measurements of Corning A provide relatively consistent results in regarding the NIST standards. The heterogeneous structure of the samples may also affect the results. These two SRM standards were previously subjected to destructive analyses many times with the LA ICP-MS technique, hence the surfaces of these standards were ablated with the laser, which led to the formation of micro-craters. As a result of the external calibration process, we measured the set of samples with 30 s of radiation. With this instrument, the elemental compositions were reported semi-quantitatively in wt% and/or ppm, and the mean values were calculated as well as the standard and relative standard deviation factors (see Tables 1–3). Each measurement point, which was numbered from one (#1) to ten (#10) for each tile, was shown in the binary and ternary scatter graphs by plotting the distribution of the oxide variation normalized by SiO_2. The normalization procedure using the major element signal (Si) [30–33] or signals from the cathode (Rh, Ag . . .) [57] aims at reducing the errors that occurred due to the variance of the distance of instrument tip to the surface artefact. The data obtained from the measurement of the body, transparent glaze, and blue decor are listed in Tables 1–3, as well as the standard deviation, which allows identifying the variations in terms of the composition, grain size, and thickness of the layers. For semi-quantitative evaluation purposes, the K-alpha emission lines of Mg, Al, Si, K, and Ca, the transition metal elements (Ti, V, Cr, Mn, Fe, Co, Ni, Cu, Zn, and As) and trace elements (Rb, Sr, Zr, Ba, and Bi), as well as the L spectral lines of lead and tin, were taken into consideration. The representative major, minor, and trace elements vary depending on the measurement layer (body, decor, and glaze matrix, Figure 3).

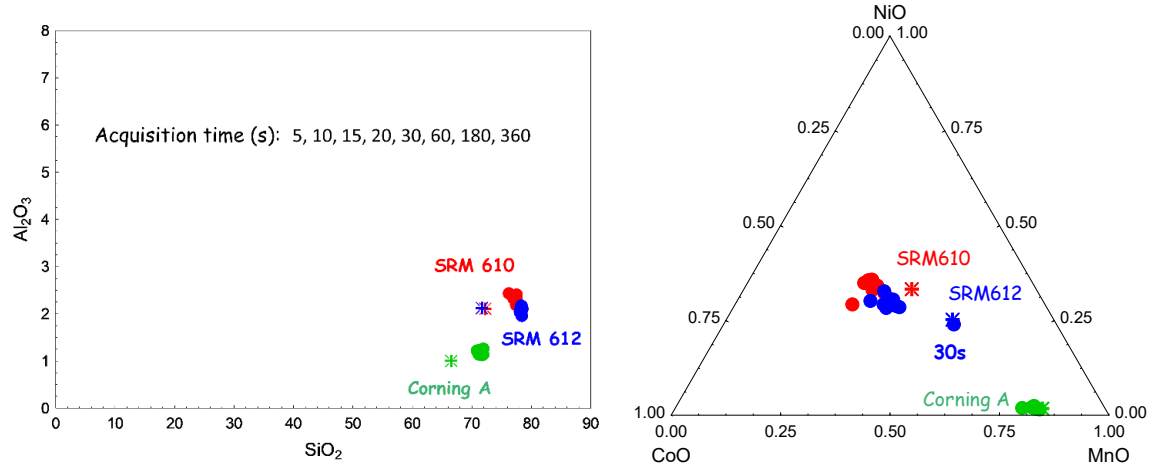

(**a**) (**b**)

Figure 2. (**a**) Binary scatter plots of Al_2O_3 versus SiO_2 and (**b**) ternary scatter plots of CoO-MnO-NiO showing the analysis points of different acquisition times (between 5 and 360 s) in comparison with the elemental compositional data (*) of the reference materials derived from the literature [55,56]. For an easy comparison, the same scale of x- and y-axes is used for the tiles studied in this paper.

Table 1. Mean elemental composition measured by p-XRF for the body on different spots and corresponding standard deviation, absolute (SD), and relative (RSD).

Body	Data	Mg	Al	Si	K	Ca	Fe	*Rb* *	*Sr* *	*Zr* *	*Ba* *	Pb	*Bi* *
IZN/15	Mean	1.23	2.80	36.67	0.96	1.87	1.06	*40*	*90*	*40*	*230*	0.93	*30*
	SD	0.15	0.24	0.99	0.09	0.29	0.18	*0.000*	*0.001*	*0.001*	*0.002*	0.25	*0.001*
	RSD	**12.58**	**8.66**	**2.69**	**9.29**	**15.49**	**16.64**	***12.52***	***8.48***	***15.78***	***10.26***	**26.65**	***24.43***
IZN/16	Mean	1.55	2.29	35.42	0.90	4.21	0.88	*50*	*140*	*90*	*300*	1.57	*80*
	SD	0.25	0.31	0.77	0.06	0.73	0.06	*0.001*	*0.001*	*0.001*	*0.005*	0.30	*0.002*
	RSD	**16.27**	**13.72**	**2.17**	**6.65**	**17.37**	**7.04**	***14.06***	***8.15***	***10.89***	***17.91***	**19.09**	***23.08***
IZN/17	Mean	1.37	3.01	34.78	1.01	2.69	1.15	*50*	*110*	*50*	*350*	1.43	*50*
	SD	0.15	0.35	1.08	0.13	0.44	0.12	*0.001*	*0.001*	*0.000*	*0.012*	0.2	*0.001*
	RSD	**10.89**	**11.51**	**3.10**	**13.10**	**16.25**	**10.83**	***12.66***	***11.01***	***9.79***	***35.21***	**13.79**	***21.25***
IZN/19	Mean	1.70	2.80	35.37	1.02	3.50	1.22	*40*	*170*	*50*	*270*	1.04	*40*
	SD	0.13	0.35	0.74	0.10	0.43	0.12	*0.001*	*0.001*	*0.001*	*0.004*	0.36	*0.001*
	RSD	**7.76**	**12.40**	**2.09**	**9.60**	**12.39**	**9.89**	***16.02***	***6.79***	***17.33***	***14.24***	**34.54**	***33.87***

* Rb, Sr, Zr, Ba, and Bi content in *ppm*; others in wt%; Na not measured with p-XRF.

Table 2. Mean elemental composition measured by p-XRF for sherd glazes on different spots and corresponding standard deviation, absolute (SD) and relative (RSD).

Glaze	Data	Mg	Al	Si	K	Ca	Ti	V	Sn	Sb	*Ba* *	Pb	*Bi* *
IZN/15	Mean	0.76	0.73	24.52	0.66	1.17	0.18	0.24	0.26	0.19	*600*	33.80	*690*
	SD	0.19	0.15	0.85	0.11	0.30	0.10	0.08	0.03	0.02	*0.02*	2.74	*0.008*
	RSD	**25.16**	**20.42**	**3.45**	**16.60**	**25.74**	**53.31**	**34.42**	**10.58**	**11.76**	***35.51***	**8.10**	***12.16***
IZN/16	Mean	0.35	0.35	28.37	0.95	0.74	0.10	0.11	2.42	0.05	*500*	25.02	*710*
	SD	0.18	0.05	0.42	0.15	0.07	0.02	0.10	0.08	0.01	*0.01*	0.70	*0.012*
	RSD	**49.59**	**14.78**	**1.49**	**15.43**	**10.08**	**15.22**	**91.31**	**3.16**	**9.99**	***24.72***	**2.79**	***16.64***
IZN/17	Mean	0.77	1.11	24.51	0.89	1.03	0.15	0.24	0.36	0.10	*500*	32.91	*670*
	SD	0.11	0.47	1.51	0.24	0.21	0.04	0.09	0.05	0.01	*0.01*	3.64	*0.012*
	RSD	**13.60**	**42.40**	**6.16**	**26.79**	**20.65**	**27.35**	**36.01**	**13.99**	**12.81**	***23.85***	**11.05**	***17.52***
IZN/19	Mean	1.10	0.67	17.53	0.63	2.54	0.54	0.29	0.23	0.40	*600*	41.93	*840*
	SD	0.34	0.17	2.72	0.07	0.44	0.52	0.03	0.03	0.04	*0.03*	4.95	*0.012*
	RSD	**30.68**	**25.61**	**15.54**	**10.37**	**17.39**	**97.11**	**11.02**	**14.90**	**10.74**	***45.23***	**11.80**	***14.16***

* Ba and Bi content in *ppm*; others in wt%.

Table 3. Mean elemental composition (wt%) measured by p-XRF for blue glazed areas on different spots and corresponding standard deviation, absolute (SD), and relative (RSD).

Blue	Data	Si	V	Cr	Mn	Fe	Co	Ni	Cu	Zn	Sn	Pb	Bi
IZN/15	Mean	23.60	0.28	0.04	0.01	0.26	0.04	0.02	0.23	0.01	0.28	36.02	0.10
	SD	0.27	0.01	0.01	0.01	0.02	0.01	0.01	0.14	0.00	0.01	0.52	0.01
	RSD	**1.16**	**3.10**	**12.48**	**47.42**	**8.13**	**32.55**	**32.55**	**63.29**	**14.37**	**4.53**	**1.43**	**14.93**
IZN/16	Mean	28.17	0.10	0.04	0.02	0.30	0.03	0.01	0.36	0.01	2.42	25.25	0.11
	SD	0.50	0.10	0.02	0.01	0.02	0.01	0.00	0.02	0.00	0.07	0.46	0.01
	RSD	**1.79**	**100**	**38.04**	**24.19**	**5.93**	**17.01**	**25.85**	**6.38**	**18.88**	**3.08**	**1.81**	**12.65**
IZN/17	Mean	23.77	0.25	0.04	0.04	0.30	0.05	0.02	0.16	0.01	0.38	34.40	0.11
	SD	1.00	0.08	0.01	0.01	0.02	0.01	0.00	0.04	0.00	0.03	2.53	0.01
	RSD	**4.22**	**33.58**	**15.02**	**16.62**	**5.50**	**15.10**	**19.16**	**28.17**	**13.60**	**8.61**	**7.35**	**10.23**
IZN/19	Mean	17.15	0.29	0.09	0.04	0.44	0.03	0.02	0.36	0.02	0.23	43.27	0.08
	SD	1.46	0.02	0.05	0.01	0.09	0.01	0.00	0.04	0.00	0.02	2.49	0.01
	RSD	**8.49**	**6.12**	**54.21**	**20.28**	**20.74**	**26.11**	**20.84**	**11.03**	**7.79**	**9.31**	**5.75**	**10.65**
IZN	**RSD_{max}**	**8.5**	**100**	**54**	**47**	**21**	**33**	**33**	**65**	**19**	**9**	**7**	**15**
Ref [3]	**Error** *	**<15**	**-**	**-**	**<40**	**<70**	**<65**	**-**	**<80**	**150**	**<25**	**>50**	**-**
	Err/RSD	**6**	**-**	**-**	**10**	**18**	**-**	**-**	**8**	**5**	**3**	**28**	**-**

* From oxide data [3].

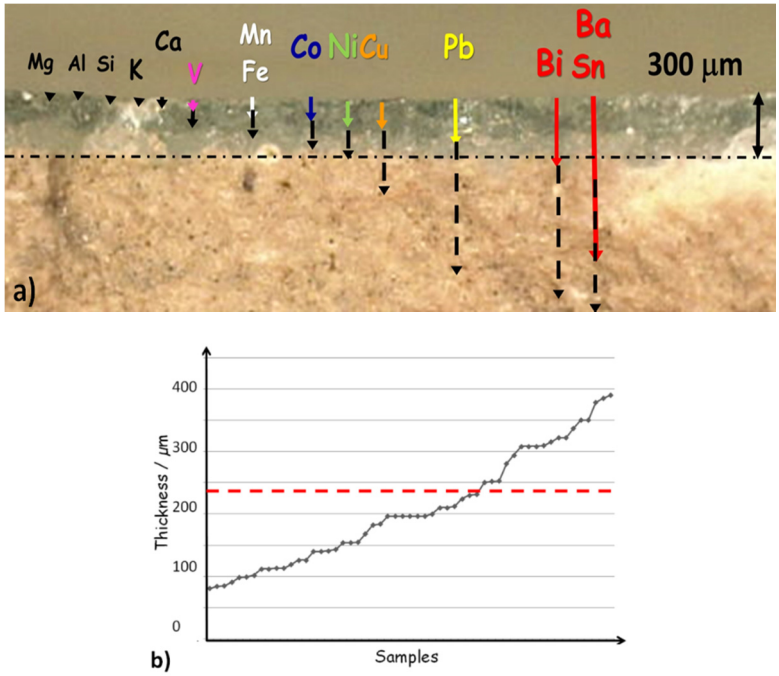

Figure 3. (**a**) Comparison of the minimum (PbO pure matrix, solid line arrow) and maximum (SiO_2 matrix, dashed line arrow) X-ray penetration depths for low-Z (Mg, Al, Si, K, and Ca) and high Z-elements (Pb, Sn, and Ba for the glaze; V, Mn, Fe, Co, Ni, Cu, and and Bi for the blue coloured area) in a glazed ceramic; (**b**) increasing variation of glaze thicknesses for the same set of Iznik ceramics. See Figure A5 for the frequency distribution of the glaze thickness.

2.3. Errors and Representativeness of the Measurements

Unfortunately, the measurement of the low-Z elements with p-XRF constitutes some problems, either very light elements (Na, O, C, and B) cannot be measured, or the measurement is very limited (Mg, Al, and Si) from the top toward the inner surface of the sample (Figure 3a), and this can undergo surface cation leaching and corrosion [58]. Fluxing elements (K, Na, Ca, and B), which are required to melt the glass and glaze, belong to the light elements group. The measurement of the glass standards show that the error rate varies between 75% and 850% for Mg and 6.5–9.5% for Si. Pb is also a major fluxing element. As sketched in Figure 3a, the penetration depth of the X-ray beam, which is used to measure K (and L) lines, is small, similar, or larger than the thickness of the glaze, which varies between ~100 and 400 µm for Iznik ceramics (Figure 3b) and the absorption is found to increase with the PbO content.

The number of elements used as colouring agents, dissolved in the (amorphous) glaze or pigment dispersed in the glaze, is always limited and depends on the colouring power. For instance, due to its high colouring power (absorption in the middle range (~500 nm) of the visible spectrum, where human eye detection is at the top [59]), 0.1 to 0.5 wt% of CoO gives a dark blue colour and 0.01 wt% can be sufficient to give light blue [3,32,33]. Other metal transition elements (Mn, Fe, Ni, and Cu) are also important colouring agents, with less power of colouration due to their main absorption occurring before or after the maximum sensitivity of the human eye. Consequently, their amount is generally higher than that of cobalt (up to a 1 wt% or more) when they are used as colouring agents. But the amount is strongly decreased when these elements are found only as impurities of the element selected as a colouring agent. Nevertheless, the penetration of the photons is sufficient to analyse the colouring elements in and under the glaze (part of the decor can be drawn on the body (on over a slip) before the deposition of the glaze (and below)). p-XRF is thus well adapted for the study of coloured glazes. Penetration of the energetic X-rays used to determine heavy elements such as tin (the main opacifying agent of ancient, glazed pottery) is much larger than that of the glaze. Tin is rather rare and costly and

thus absent (or found only as very small traces) in the lead-containing frit (crushed glass) present in the composition of Iznik bodies, so it does not affect the representativeness of the measure. Although the penetration depth of lead (1.13 mm) is also larger than the thickness of the glaze layer, the measurement accuracy of the glaze is not affected by the penetration of X-rays, because the lead content (see Table 1 for the sherds IZN/15, IZN/16, IZN/17, and IZN/19) in Iznik pastes is much lower in the composition of the body (1–4 wt%) than in the glaze [60].

The amount of element in the probed volume is also an important factor. As shown didactically in Figure 4, Si and Al are the major elements that build the phase structures of the ceramic body and glaze. Measurement of the major elements is not affected by the Limit of Detection (LOD), and it can be anticipated that the heterogeneity of the artefact in the probed volume will determine the standard deviation measured for a given artefact. The LOD might be considered for colouring elements and associated impurities, thus the low amount of these elements and their heterogeneous distribution in the probed volume play an important role. The beam surface of the handheld instrument (1 cm^2) is large, though an analysis from a smaller surface is possible with the later generation instruments (~1 mm^2) [61], but a motorised XYZ stage is required that limits the use of these instruments outside.

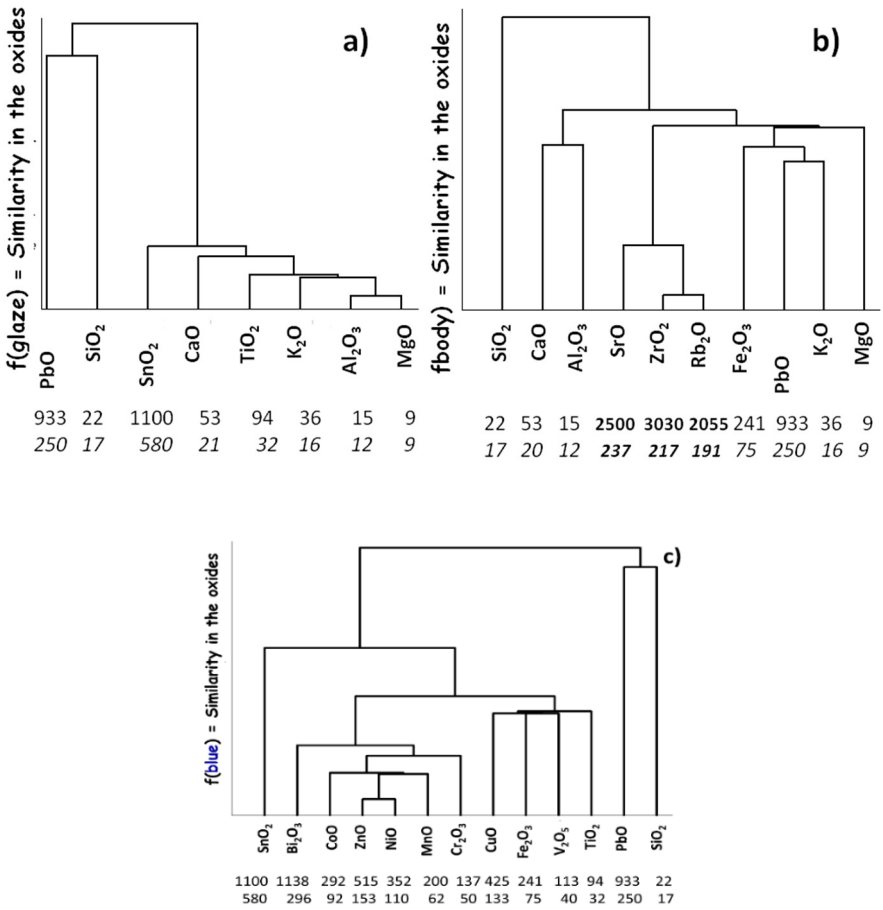

Figure 4. Tree clustering dendrograms of glaze (**a**), body (**b**), and blue coloured layer (**c**), which show the representative oxide compositions; below, the maximum (upper line, pure SiO_2 matrix) and minimum (pure PbO) penetration depth values in microns are given. The Euclidian clustering level classifies well the major (Si, Ca, and Al in the body; Pb, Si in the glaze), the minor elements (fluxing and colouring agents), and traces (e.g., Sr, Zr, and Rb in the glaze).

Binary and ternary scattering plots, which represent XRF data of the studied tiles (each sherd shown in different coloured labels, see the legend of Figure 5) were drawn with the software Statistica Academic Version 13. The hierarchical clustering diagrams (also known as dendrograms) were drawn

with the same software. The similarity in the variables was calculated by "single linkage" amalgamation and Euclidian distances. Additionally, the software of Microcal™ Origin® version: 6.0 is used for the combination of the old and current data.

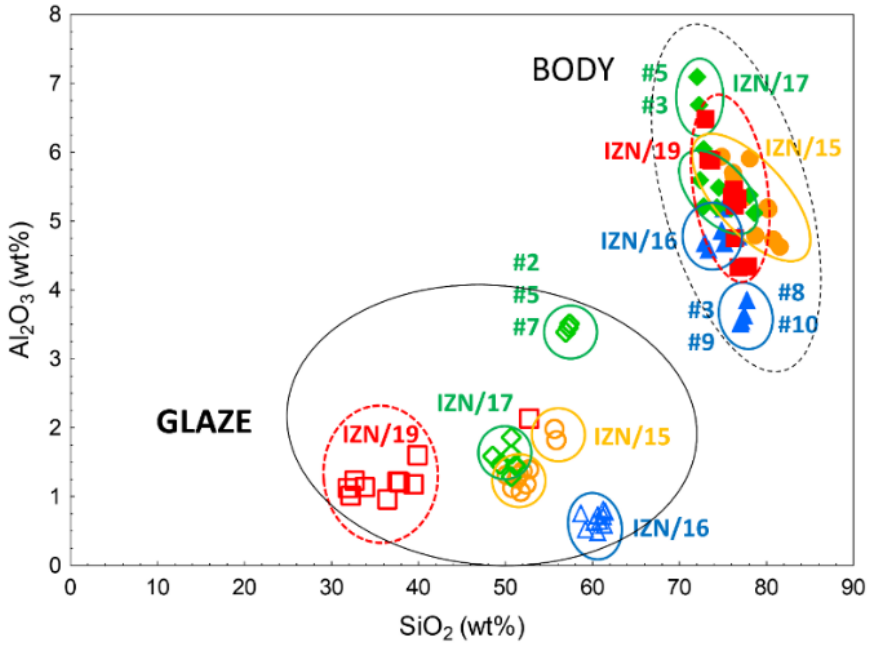

Figure 5. Binary scatter plots of Al_2O_3 (wt%) versus SiO_2 (wt%) in the glaze and body of the tiles IZN/15 (orange circle), IZN/16 (blue triangle), IZN/17 (green diamond), and IZN/19 (red square). Open labels represent the data obtained from the glaze, and the solid labels represent the body analyses (#X: spot number, see Appendix A). Ellipses are drawn as a guide for viewing for comparison with data obtained on reference materials (Figure 2).

3. pXRF Methodology

Before starting the campaign of measurements with p-XRF, the instrument was tested with the appropriate reference standards. The previous similar studies show that for the ceramic analyses, both glasses and red mud standards are used to reveal the reliability of the technique [29,30]. Therefore, two standards of NIST (SRM610 and SRM612) and a Corning A glass standard were measured with different acquisition times and different built-in calibration modes. Table A1 in the Appendix A presents the elemental composition of the standards recorded at 5, 10, 15, 20, 30, 60, 120, 180, and 360 s. The amount of Mg, a very low Z element, is seen to be quite high in comparison with the high precision analysis of the reference standard with the laboratory-scale instruments. The error rate of Mg is 842%, 0%, and 75% for NIST SRM610, SRM612, and Corning A, respectively. However, for Si, the error rate is below 10%, which is acceptable for a reliable measurement. For SRM, 610 is 6.5%, for SRM612 9.3%, and for Corning A standard, the rate is 7.8%. However, K and Ca, used as fluxing agents in the composition of the glaze, have similar concentrations, which allows a better classification of the samples. Additionally, the variation in the time-dependent measurement of the same standard is very narrow, showing the consistency of the semi-quantitative XRF data. If a new configuration will allow the use of a tripod with the instrument, 120 s of acquisition time will be also satisfactory for the determination of the elemental composition of the body. Instead, 30 s of acquisition time is the optimal parameter for the quantification of trace elements found in the coloured areas, in this case the blue decor. Built-in calibration modes enable a better quantification of the XRF data, but only if they are selected properly. After optimizing the acquisition time, we tested different methods on the NIST and Corning standards. The rare earth elements mode uses higher energy, 50 keV, than the other calibration methods (45 keV), which allows a better distinction of the high Z elements to be made. In the case of

glazed ceramics, the reading of both low-Z and high-Z elements is correlatively important. Only with the Mining Light Elements method can the elements Si, Al, and Mg be determined.

4. Results—Materials: Microstructure and Elemental Composition

4.1. Body

Previous on-site studies at Iznik Tile Kilns Excavation identified three types of paste composition: (i) Group #1: the low amount of quartz (~50 wt% SiO_2) and high alumina (12–16 wt% Al_2O_3), briefly named "clayey body"; (ii) Group #2: a high amount of quartz (65–85 wt%) and low alumina (3–6 wt%), named "fritware/stonepaste"; (iii) Group #3: the medium amount of quartz (39–62 wt%), low alumina (3.6–6.3 wt%), and high amount of calcium (11–27.5 wt% CaO), described as a calcareous-rich clayey body. The tiles, which are used in this study for the statistical analyses, contain mainly 72–81 wt% SiO_2, 3.5–7 wt% Al_2O_3, and 2.1–7.8 wt% CaO, and so refer to the group classified as stonepaste #2 [32]. The visual examination permitted a certain way of distinguishing the colour variation of the paste for these three groups. The body of Group #1, which represents the earlier productions of Iznik (14th- and 15th-centuries) in the form of "brick", has a reddish appearance. Group #2, which refers to the productions of the classical period of Iznik (16th-century), is whitish, and Group #3, which corresponds principally to the later productions (end of 16th and 17th centuries), appears light beige. The tiles studied in this research are assumed to be produced between the 16th and 17th centuries. IZN/15, 16, and 17 belong to the group of "blue-and-white" productions, while IZN/19 is an example of "Rhodes" work. The colour of the paste varies from relatively dark (IZN/15, 16) to light beige (IZN/17) and off-white (IZN/19). The sherds IZN/15, IZN/17, and IZN/19 have a slip layer of around 1.5 mm in thickness, while the slip layer of the sherd IZN/16 is thinner.

The mean elemental compositions of the elements and standard deviations are given in Table 1, and the complete results obtained from ten single points of measurement are shown in Table A2. Corresponding oxide compositions are given in Appendix A, but we must underline that a major element is not measured, which is sodium. It should be noted that the glaze and body components of ceramics are formed in oxide structures (as presented in Figures 5 and 6), but the penetration depths are calculated as a function of the absorption parameter for the representative elements found in the mixture of the raw materials used for the body and lead-based glaze, as well as their thicknesses (schematised as silica and lead oxide respectively in Figure 4).

Penetration depths are given for both pure silica and lead oxide, the first model being representative of the body; the penetration depth in the glaze will be intermediate between that calculated for pure silica and lead oxide. Moreover, Figure 3 visualizes the differences of the constituents between body, glaze, and (blue) coloured glazed areas.

The binary scatter plots of Al_2O_3 (derived from the clay) versus SiO_2 (derived from the quartz) represent different groups of Iznik productions (Group 1–3) concerning the elemental composition of the glaze and body [32,33]. The addition of the new data in the representative plot (see further) will lead to identifying in which group the new materials are included. Figure 5 shows that the variation of the matrix composition in the glaze is larger than that in the body. It also represents the heterogeneity of the glaze layer, which is higher due to the partial differences of the thickness, composition of the major and minor constituents, and existence of surface defects. The subgroups, which represent the differences of the measurement points, are evidenced in the analysis of both glaze and body layers. In the case of body analysis, the dimensions of the porosity and presence of different mineral phases affected the results and lead to subgrouping. Glaze subgrouping is associated with defects observed with the p-XRF camera.

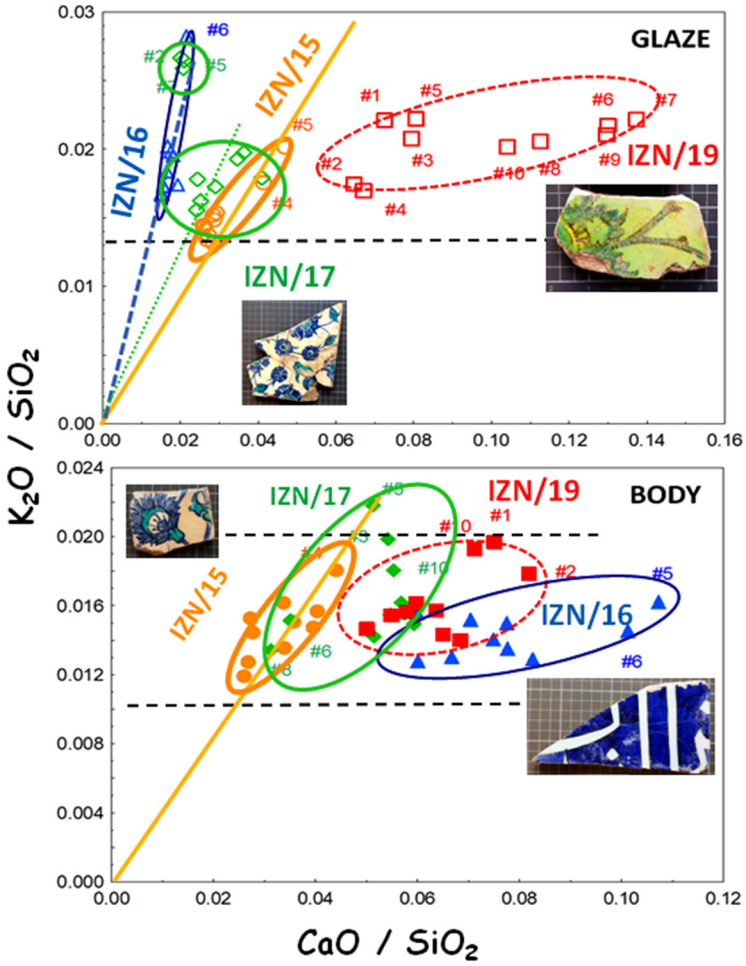

Figure 6. Binary scatter plots of K_2O/SiO_2 versus CaO/SiO_2 in the glaze (**upper**) and body (**bottom**). Lines are drawn as a guide for viewing (See Figure 4 for labels, #X: spot number, see Appendix A).

Examination of Figure 5 shows that variation of about ± 5% for SiO_2 wt% and of ± 0.5% for Al_2O_3 wt% can be considered as the variability arising from the heterogeneity of the tiles. Comparison between Figure 2 (reference materials) and Figure 5 (Iznik materials) clearly shows that the scattering of the values arises from the local heterogeneity of the artefacts. The variation is a little smaller than the RSD_{max}, because some discrepancies are correlated to defects observed at the camera before the measurements (Figure A2, IZN/15: #4, #5; IZN/17: #2, #5, #7; IZN/19: #2, #4, #5). The LOD value of potassium (K_2O/SiO_2 ~< 0.01) was found to be almost the same in the glaze and body layers measured with the p-XRF instrument in comparison with SEM-EDS analyses carried out at the laboratory [62]. The content of potassium oxide in the body appears quasi-independent of the amount of calcium for the tiles IZN/16 and 19, by showing that K_2O is not related to the composition of the clay found in the body, but may refer to an impurity associated with quartz (potentially K-feldspar). On the contrary, the body composition of the tiles IZN/15 and 17 contains proportionally potassium and calcium oxide, and these may come from the clay. The large distribution of the amount of calcium oxide found in the glaze of IZN/19 reveals explicitly the dull appearance of the glaze. Here also (Figure 6), the subgroupings of the measurement points (for example for IZN/17, #2, 5, and 7) in the glaze refer to the tarnished surfaces. Errors are ± 0.025 for the CaO/SiO_2 ratio and 0.01 for the K_2O/SiO_2 ratio.

4.2. Glaze

The glaze of the Iznik tiles belongs to the lead-alkali type (20–45 wt% PbO, 8–14 wt% Na_2O) with a tin oxide content of 0.1 to 8 wt% [49,62]. Unfortunately, p-XRF cannot measure the Na content.

In Table 2 and in the Figure 5 diagram, the lower content of SiO_2 and Al_2O_3 in comparison with the body composition is obvious and results from the relatively large amount of PbO present (25–40 wt% PbO, Table A3). The thickness of the glazes may be divided into two groups: namely, thick and thin. The two tiles, IZN/16 and 19, contain a glaze of 0.30 mm in thickness. However, the glazes of the tiles IZN/15 and IZN/17 have a thickness of around 0.15 mm. From the binary scatter plots shown in Figure 7, we observed that the tiles IZN/15 and IZN/17 have a similar but larger variation of lead oxide (min 27 wt%–max. 36 wt% PbO), while IZN/16 has a more homogeneous glaze layer that contains 24–27 wt% PbO. Moreover, the (dissolved) tin oxide content of IZN/16 is around 2.4 wt%, which refers to its intentional addition in the glaze. However, IZN/15 and IZN/17 contain dissolved tin oxide less than 0.5 wt%, which may be an impurity of lead. Previous studies demonstrated that tin oxide content decreases by centuries, from the 15th to the end of the 16th century, and the productions of 17th centuries do not contain any tin in both the transparent glaze and coloured decor [32,33].

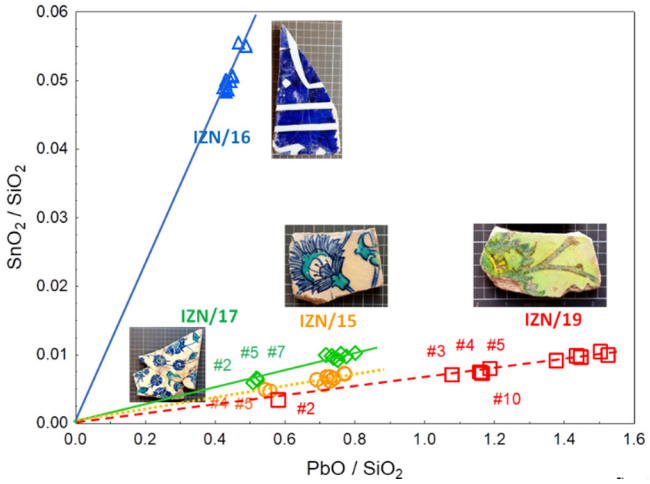

Figure 7. Binary scatter plots of SnO_2/SiO_2 versus PbO/SiO_2 in the white-coloured areas of the glaze by showing the representative images of the sherds (#X: spot number, see Appendix A).

The standard and relative standard deviation (RSD) factors are calculated for the major (Si, Pb, and wt%), minor (Mg, Al, K, Ca, Ti, V, Sn, Sb, and wt%), and trace elements (Ba, Bi, and ppm) found in the transparent glaze (Table 2). The low value of RSD Si of IZN/16, which is found to be 1.49%, confirms the observation of the glossy finish of the glaze. Therefore, the dispersion of the results is smaller than in the other three tiles. In contrast, the tile IZN/19, which has a dull surface due to the corrosion and/or improper firing, has a bigger RSD for Si (15.5%). Moreover, the variation of tin is also smaller for the tile IZN/16 (RSD Sn: 3.16%), which refers to its intentional addition as an opacifier. In the other tiles, the presence of tin appears probably as an impurity in the lead source. The physical properties of the surface analyzed directly affect the consistency of the measurements of the composition. The flatness of the surface, the absence of porosity, and the smaller dimensions of the grains lower the standard deviation, and thus this increases the reliability of the measurements with p-XRF. Furthermore, it is observed that the major elements found in the glaze are not affected by the thickness of the layer (0.15 µm for IZN/15 and IZN/17; 0.30–0.35 µm for IZN/16 and IZN/19).

For the glaze analysis, the differences in the composition derived from the quality of the surface, which turned the transparent glaze to yellowish colour and changed the elemental composition. The higher content of silica (SiO_2) and lower content of alumina (Al_2O_3) may decrease the resistance to corrosive attacks that have occurred under the soil [63]. Therefore, the corrosion resistance of IZN/16 is less than the other sherds. The less-well preserved glazed surface of the other samples is thus due to their pristine poor state: they are rubbish, and this has certainly been the reason for their rejection. Hence, an integrated camera in the p-XRF instrument is preferred for the characterization of ancient

ceramics to visualise the focused zones and choose the different facies before each measurement of the glaze, coloured areas, and body (Appendix A).

The binary scatter plots of SnO_2 versus PbO show the linear correlation of lead and tin, which refers to the use of the same raw material and is only different for the glaze of IZN/16. The Pb/Sn ratio is found to be 10.3, which confirms the literature data presented for opaque white glazes [49,64]. A further study with Raman spectroscopy (non-invasive) or SEM-EDS (micro-destructive) is needed to see if the tin remains dissolved or precipitated in the form of cassiterite. The other three tiles contain almost no tin, which may not have been added intentionally, but is present as an impurity in the lead.

4.3. Blue Colouring Agent

Colouring a glass (i.e., a glaze) is an advanced technology that uses some rather rare elements. This is the case for the blue colour that can be obtained only by three routes, namely, cobalt and lapis lazuli in the past and V-doped zircon for a few decades more recently [65]. Consequently, long-distance trading was established both for lapis lazuli [66] and cobalt [65]. The main sources of cobalt are European [67], Persian [68], and Asian [69,70]. It is reported that ancient Chinese texts mention the importation of different types of "blue ores" that have been coming from Islamic countries and/or from Europe [38]. Due to different orogenesis, the composition of Asian and European/Persian ores are different. The latter are arsenic salts, although the Asian sources are arsenic-free and generally richer in Mn (and Fe) than in Co [65,66], with Mn/Co ratio up to 5. The presence of Mn and Fe impose a firing under reducing atmosphere to produce a blue colour. Both have associated transition metals (Fe, Mn, Ni, Cu, and Co), but the relative ratios vary and some other elements like Bi or Zn are also identified [65–78].

Before the chemical analyses were undertaken, a visual examination of the sherds revealed the differences in the hue of the blue-coloured areas, which is darker in IZN/16 compared to the other tiles IZN/15, IZN/17, and IZN/19. The elemental measurements (Table 3; corresponding oxide compositions in Table A4) showed that these three tiles contain a similar amount of Co (0.03 to 0.05 wt%), Mn (0.01 to 0.04 wt%), Fe (0.3 to 0.4 wt%), Ni (0.02 to 0.03 wt%), and Zn (0.01 to 0.02 wt%) without arsenic, but the copper content slightly varies between 0.16 wt% (IZN/17) and 0.36 wt% (IZN/16 and IZN/19). Even the compositions are relatively similar, the ratios of the elements (Co/Ni, Co/Mn, etc.) may be evidence of more specific findings. Co/Ni ratios for IZN/15, IZN/16, IZN/17, and IZN/19 are, respectively, 2, 3, 2.5, and 1.5, while the Co/Mn ratios are 4, 1.5, 1.25, and 0.75.

The data of Liu et al. [3], measured on blue glass beads, i.e., a homogeneous and infinite sample, shows that the error of p-XRF measurement in comparison with ICP-AES is small for the major elements, varying between 1% and 12% and much higher for minor and trace elements, which change between 10 and 400%, the largest values being observed for the light and trace elements. Since the volume probed for the light elements (Figure 3) will be small, the results may be affected by corrosion. Indeed, the smallest RSDs regarding the glaze elements are measured for the sample exhibiting the highest gloss (IZN/16), and the largest for that exhibiting a degraded surface (IZN/19, Figures 5–7), as observed for the "white" areas. The major, low-Z elements such as Si have a smaller RSD value than the transition metals (Cr, Mn, Co, Ni, Cu, and Zn), and the RSD is medium for Sn and Pb, which shows a better homogeneity in comparison with the dissolved colouring agents in the glaze or underglaze. Similar errors are observed in our samples. The maximum RSD factor measured for Si on an Iznik tile is 8.5% (Table 3). We can expect that the error will be similar for the second major element, Pb; here, the RSD_{max} is equal to 7%, close to the value observed for Sn (RSD_{max} = 9%). RSD_{max} values measured for cobalt and associated elements range between 15% and 100% of the same order of the error given by Liu et al. [3] for these elements.

The dispersion of the blue colourants shown in the ternary scatter plots of CoO-NiO-MnO is comparable for all the tiles except IZN/19. Additionally, the variance of IZN/15 is slightly higher than IZN/16 and IZN/17. For these elements, the probed volume is of the same order of the glaze thickness and this is consistent with the similar dispersion of the data shown in Figure 8 and Table 3.

No differences can be related to the varied thicknesses (IZN 16 & IZN19 = 300 μm; IZN 15 & IZN 17 = 150 μm). Note that the elongation of the ellipses drawn in Figure 7 is plotted alongside the lines between fixed Co/Ni and Co/Mn ratios. This could be due to the occurrence of a mixture between two cobalt ores, respectively, Ni and Mn-rich, from different origins or to the presence of different compositions in the ore mined in the same location (see further). In contrast, significant differences are observed in the graph of Bi_2O_3-CoO-ZnO by revealing a very narrow variation for IZN/16, like that already observed in the binary scatter plots of SnO_2 versus PbO. This is assigned to the high quality (preparation and preservation) of the IZN/16 glaze. The significant content of ZnO found in the blue coloured area of IZN/19 relates directly to the yellowish colour of the glaze in which Zn is added in the pyrochlore solid solution ($Pb_{2-X}M'_XM_{2-Y}M''_YO_{7-\delta}$ with M, M'' = Sb, Sn, Fe, Si, Zn; M' = RE) that gives the characteristic Naples yellow colour [61].

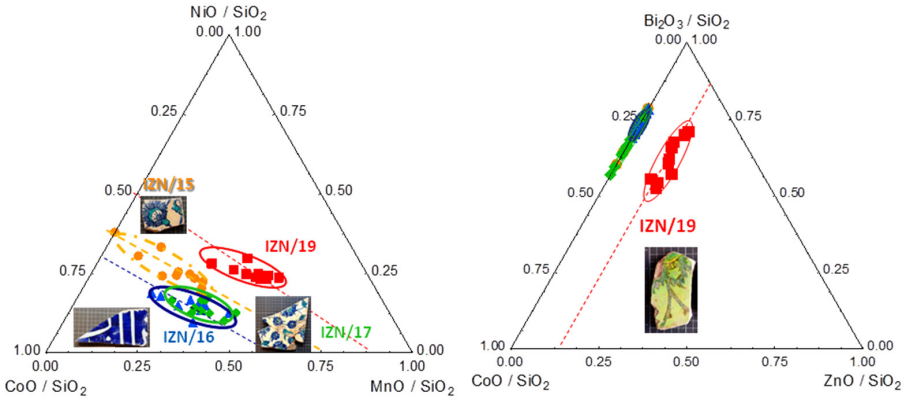

Figure 8. Ternary scatter plots of CoO, NiO, and MnO (**left**), and CoO, Bi_2O_3, ZnO (**right**) normalized by SiO_2 found in the blue coloured areas (#X: spot number, see Appendix A). Lines and ellipses are drawn as a guide for viewing.

The amount of copper appears more random, being narrow only for the IZN/16 sample (Figure 9). There is not a direct relationship with the Co content. This can be explained by the fact that copper occurs as an impurity in other raw materials. The highest content is observed for the IZN/19 glaze in which Bi is detected.

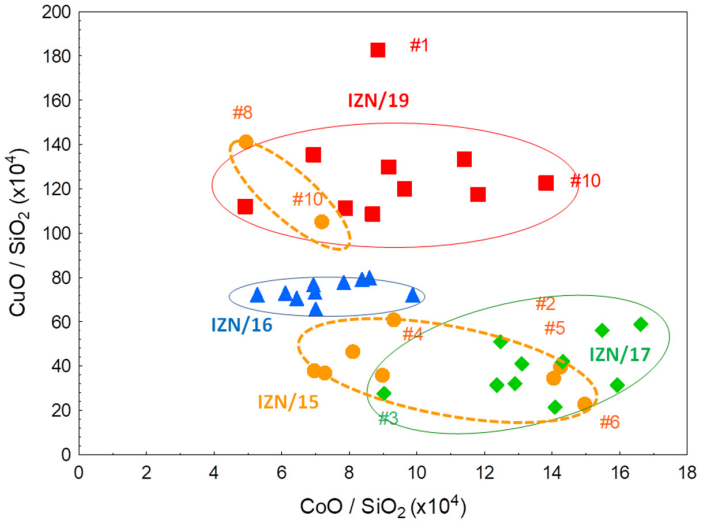

Figure 9. Binary scatter plots of CuO versus CoO normalized by SiO_2, found in the blue-coloured areas (#X: spot number, see Appendix A). Lines and ellipses are drawn as a guide for viewing.

5. Discussion: Comparison of the Results with the Previous Measurements

The results of the previous measurements, which were performed on the Iznik tiles preserved as the wall revetments of the holy places in Edirne [33] and unearthed materials of the previous excavation seasons [32], are also included in Figure 10 to obtain an overall assessment of the Iznik tiles produced with different technologies in different periods (mainly between the 14th and 17th centuries). The ellipses in Figure 8 are also drawn in Figure 10 to facilitate the comparison of the reference results of IZN/15, 16, 17, and 19 with the previous ones carried out at different sites (Edirne and Iznik). Data collected on different buildings from different sites are more scattered than those recorded on reference sherds, but the distribution along the lines drawn in Figure 8 was validated also in Figure 10. This plot is consistent with the use of different cobalt ores containing different ratios of Ni/Co, Mn/Co, and Bi_2O_3/CoO, which is also consistent with the literature data [32,33,65–78]. The differences in the composition of various samples are thus significant.

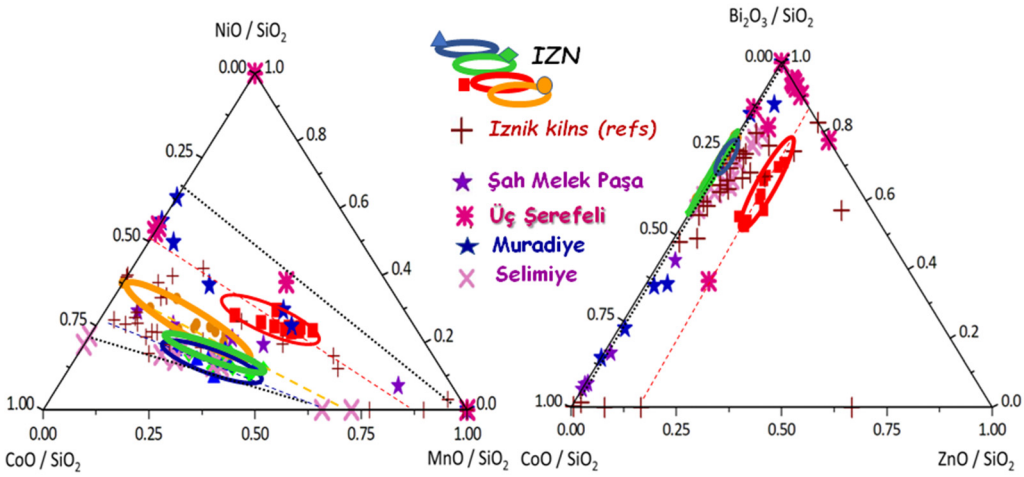

Figure 10. Comparison of the intrinsic variability measured on IZN samples with a set of measurements made on the blue areas of sherds previously excavated from Iznik kilns [32] and on tiles of Edirne mosque (Şah Melek Paşa (1429), Üç Şerefeli (1410–1447), Muradiye (1435–1436), and Selimiye (1569–1575) [33]. Ellipses of Figure 7 have been reported in the previous section.

The clustering of different groups arises from either the use of the same raw materials with different concentrations or from different ores. The specific cases of the blue pigment appeared in the wall revetments of Edirne mosques. The blue of Üç Şerefeli Mosque (1410–1447) is rich in Bi_2O_3 and NiO, while Şah Melek Paşa (1429) is richer in MnO. Some of the tiles of Selimiye Mosque (1569–1575) have a blue pigment that is rich in MnO and poor in NiO. The ratio of Al_2O_3 versus SiO_2 plotted in Figure 11 shows that the sherds studied in this paper belong to the group 2 described previously in the first study of the unearthed materials, and the dispersion of the measurements is very limited. The scattering of the glaze data is also narrow but confirms explicitly the use of different glaze technologies related to the different ceramic workshop and/or the artist. The scattering of the data is very similar.

Figure 12 shows the corresponding Euclidian hierarchical dendrogram for the content of Al_2O_3 and SiO_2 in the glaze. Lower levels are not significant. The specificity of the Üç Şerefeli tile technology is obvious, as well as the presence of two glazing technology for the Muradiye tiles. The tiles studied in this paper are similar to the tiles of Edirne's mosques, except for some blue-and-white tiles of the Muradiye Mosque. However, IZN/16 is more comparable with the tiles of the Üç Şerefeli and Şah Melek Paşa Mosques.

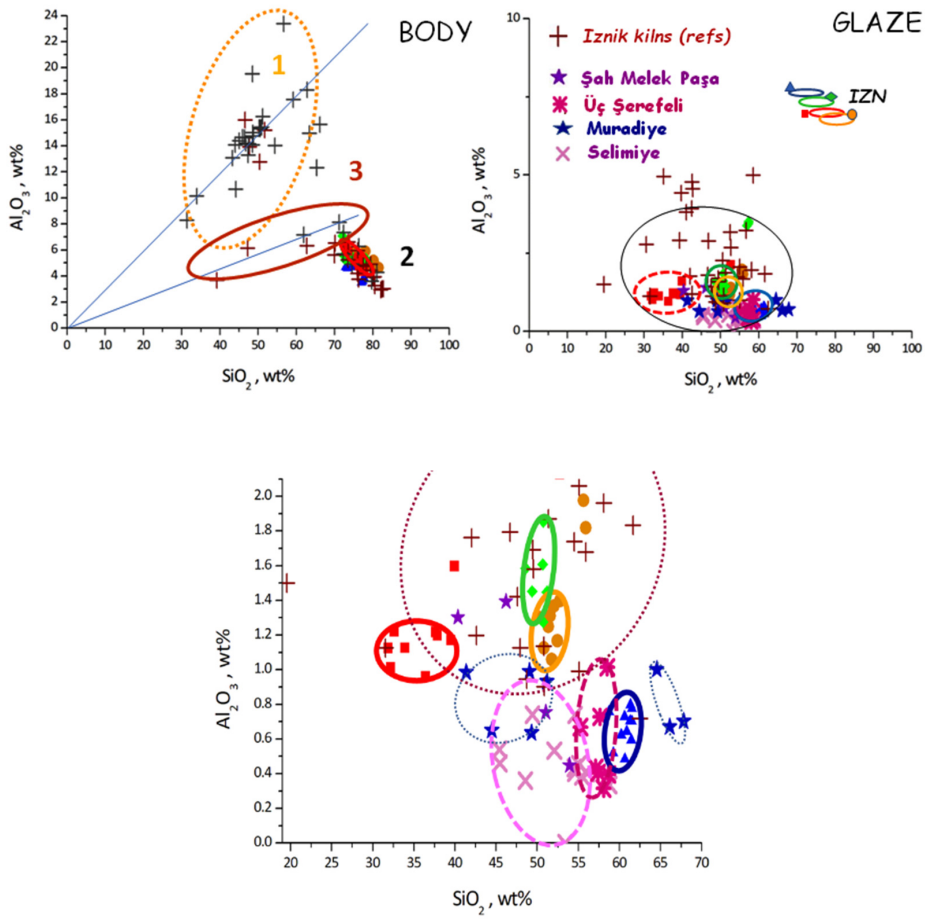

Figure 11. Comparison of the intrinsic variability measured on IZN samples with a series of measurements made on transparent, glazed, white-coloured areas and the body of sherds previously excavated from Iznik kilns and measured on-site on white glaze [32,33]. A zoomed plot is given for the glaze data (bottom right).

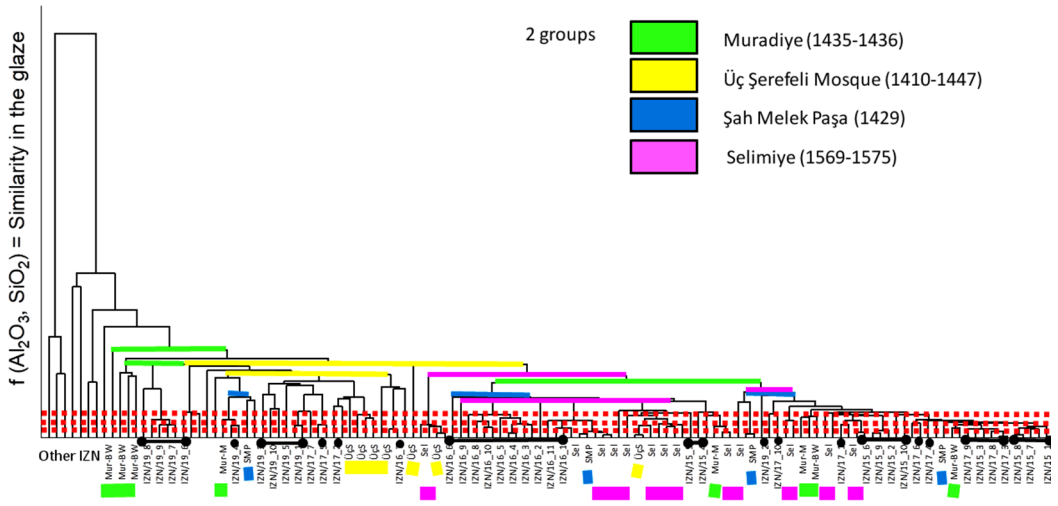

Figure 12. Clustering diagram comparing data collected on IZN samples with those collected on-site at Edirne mosques. The dotted red lines allow differentiating the levels of hierarchical clustering for the sherds examined in this study where only the higher hierarchical levels make sense. On the left side of the diagram, previous materials studied at the Iznik Tile Kilns Excavation [32] are clustered.

The reliability of the p-XRF measurements for the comparison and classification of the body and glaze layers is thus good and valid for on-site measurements. In Figure 13, the application of a mean error of about 15% for Si and Pb to the measurement data shows that previous conclusions are not perturbed and that the comparison of the Sn/Pb ratio is a good tool to follow the technological evolution of the Ottoman glazing technique and its relationship with its Seljuk precursors.

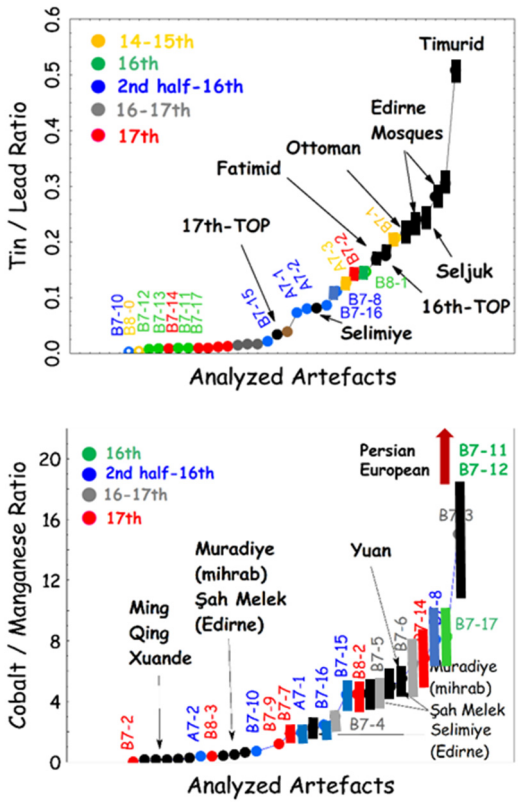

Figure 13. Comparison of the Sn/Pb and Co/Mn ratio for a series of measurements made on white and blue glazed areas of Iznik tiles [32,33]. The error bar is deduced from the present work.

The uncertainty of the measurement of the Co/Mn ratio is much more important. As visible in Figures 8 and 10, the data are scattered along lines with a variable Co/Mn ratio. The nearest cobalt source being Kashan mining, it is tempting to assume that the cobalt ores are coming from Persia. Alternative importation from Europe (Erzgebirge) has been proposed by Porter [78] when bismuth is detected, according to geological studies [67]. A study of Kashan ores by Matin and Pollard [79] shows the variation of the Mn/Co ratio from 1 to 10 as a function of the ore sample collected, which is consistent with the scattered data observed for these IZN samples. The Ni content is rather constant, which looks also consistent with the variability observed for IZN references and some Edirne mosque tiles. Here also, the Üç Şerefeli mosque tiles, which are rich in bismuth, may be made with other cobalt ores, and most likely with European cobalt ores. The estimation of the error is thus rougher, varying between 50% and 200%. An illustration of the increasing error with the decreasing cobalt content has been applied to Figure 12. This does not modify the main classification previously proposed [33].

6. Conclusions

The study of the reference unearthed ceramic samples allows the exploration of the uncertainty of p-XRF regarding the exhaustive information that corresponds to the composition measured on the glazed ceramics, even when the glaze has lost its gloss. To determine the reliability of the instrument, an external calibration procedure must be first applied before the measurement campaign. Similar reference standards of the real artefacts will be used for providing the optimum measurement conditions.

With this aim, NIST (SRM610 and SRM612) and Corning A glass standards were analysed at varied acquisition times (from 5 to 360 s) by using different built-in modes (Mining, Mining Light Elements, Soil, and Rare Earth Elements). As a result of the analyses, 30 s of radiation time is found optimal for the semi-quantitative characterization of lighter and heavier elements when the instrument is used manually under the special conditions of measurements, which are made on site with only limited accessibility. Additionally, Mining Light Elements calibration was the most accurate mode to quantify the amount of silicon and aluminum.

After the pre-measurement of the standards, four tiles were measured by focusing ten single points on each layer (comprising the transparent glaze, blue coloured area, and body). The data appear reliable for the major elements and their comparison of the elemental ratio for transition metals, the penetration depth probed being rather similar to the thickness of the glaze. We can anticipate that the analysis of pottery with a thin glaze layer (<~100 μm) will be significantly perturbed by the contribution of the sub-layer(s), slip, or body. The choice of the surface probed with a camera allows the elimination of areas that are not representative (such as defects and the mixing of coloured areas). Moreover, the proper calibration mode should be chosen for the right materials. The instrument used in this study has a rather large spot (a few mm^2), which averages the information acquired for the body (coarser grains ~x μm) and the glaze. The anisotropy of the scattering of the data in CoO-MnO-NiO measured on the blue areas is consistent with the use of heterogeneous ores such as those from Kashan Mining (Persia). Consideration of the Bi content gives a strong argument to support the use of a special cobalt source for the Üç Şerefeli mosque tiles, likely European.

Author Contributions: Conceptualization: G.S.F., P.C., B.D.A., and S.K.; methodology: G.S.F.; validation: B.D.A., G.S.F., S.K., H.A., and P.C.; resources: B.D.A., S.K., and H.A.; data curation: G.S.F.; writing—original draft preparation: B.D.A., S.K., G.S.F., and P.C.; funding acquisition: B.D.A. All authors have read and agreed to the published version of the manuscript.

Funding: This research was funded by Istanbul University Scientific Research Projects Coordination Unit, grant number: BAP SBA-2017–25651.

Acknowledgments: Tuna Eroğlu and Salih Mut from TROY-MET (Istanbul) is gratefully acknowledged for making the Hitachi X-MET 8000 Expert Geo p-XRF instrument available at Iznik Tile Kilns Excavations for on-site measurements. The authors also thank Professor Julian Henderson and Peter Winship (from Teledyne CETAC Technologies) for sending us Corning and NIST standards.

Conflicts of Interest: The authors declare no conflict of interest.

Appendix A

Appendix A.1 Analyzed Spots

Each single "studied spot" in the body, transparent glaze, and blue coloured areas is shown in Figures A1–A4.

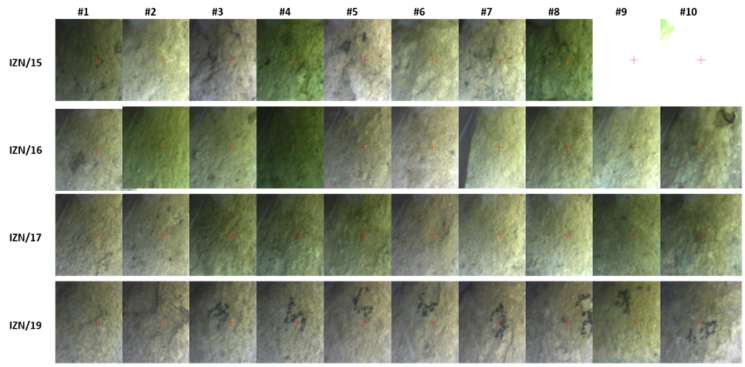

Figure A1. Representative images of the analysis spots shown with the red plus sign, counting out the first measurement (#1) to the last one (#10) in the body.

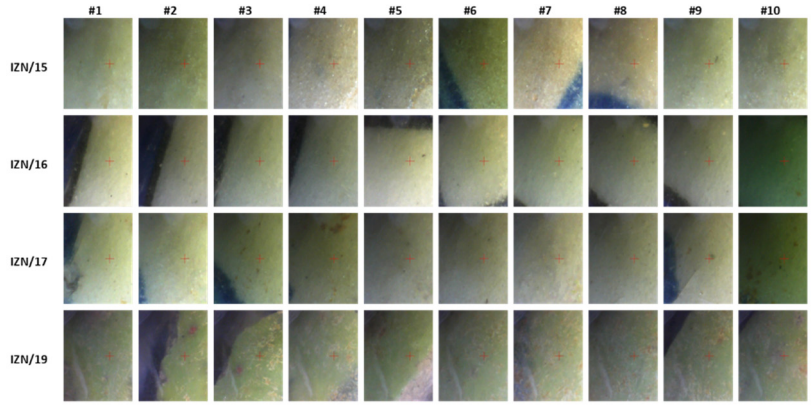

Figure A2. Representative images of the analysis spots shown with the red plus sign, counting out the first measurement (#1) to the last one (#10) in the transparent/white coloured glaze.

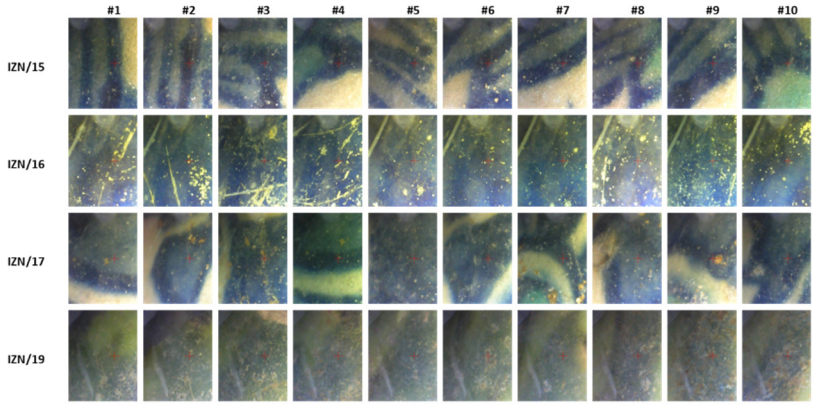

Figure A3. Representative images of the analysis spots shown with the red plus sign, counting out the first measurement (#1) to the last one (#10) in the blue coloured areas.

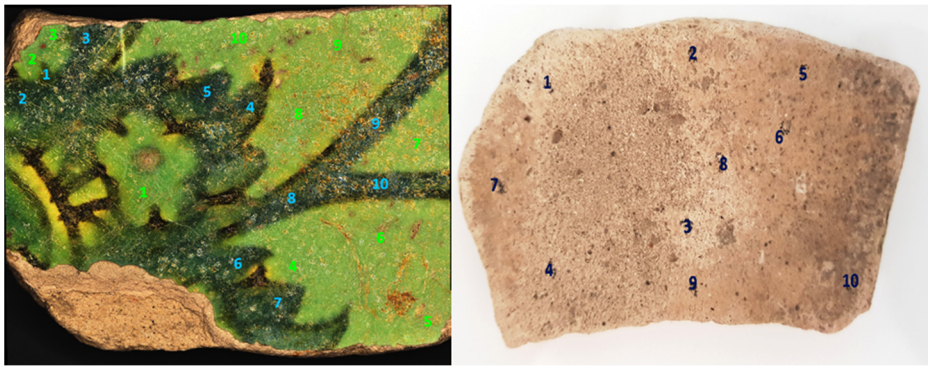

Figure A4. General view of the glazed and bodied surfaces of IZN/19 showing ten measurement points.

Appendix A.2 Glaze Thickness

The thickness of the glaze measured for a series of sherds excavated at Iznik Tile Kilns is shown in Figure A5.

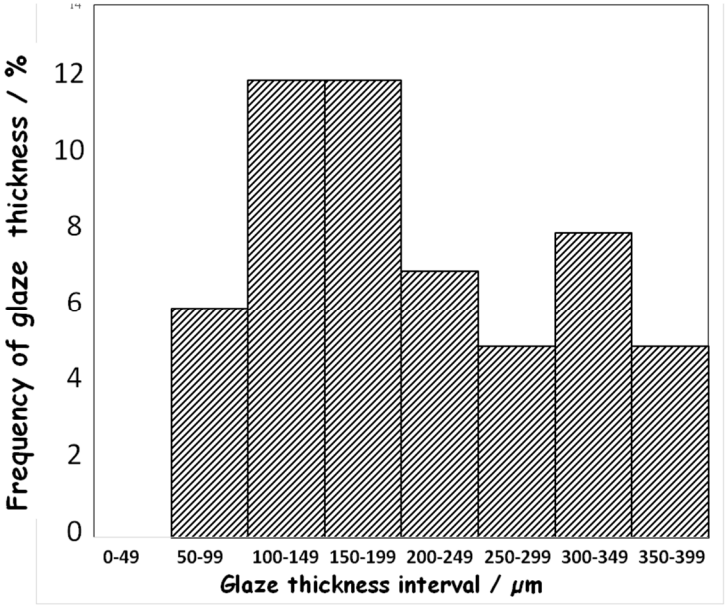

Figure A5. The frequency distribution (%) of the glaze thickness of Iznik sherds.

Table A1. XRF data (wt%) showing the measurements with different acquisitions times (5, 10, 15, 20, 30, 60, 120, 180, and 360 s) carried out on the glass standards of NIST (SRM 610 and 612) and Corning A in comparison with the data found in the literature.

Label	Acquisition Time	MgO	Al_2O_3	SiO_2	K_2O	CaO	Fe_2O_3	Rb_2O	SrO	ZrO_2	PbO
SRM610	360 s	0.65	2.34	77.39	0.26	0.00	11.00	0.00	0.07	0.13	0.65
	180 s	0.71	2.37	77.49	0.25	0.00	10.89	0.00	0.06	0.11	0.71
	120 s	0.66	2.36	77.54	0.26	0.00	10.90	0.00	0.06	0.12	0.66
	60 s	0.68	2.36	77.44	0.25	0.00	10.97	0.00	0.06	0.13	0.68
	30 s	0.66	2.32	77.03	0.25	0.00	11.32	0.00	0.06	0.12	0.66
	20 s	0.41	2.36	77.55	0.24	0.00	11.07	0.00	0.08	0.12	0.41
	15 s	0.31	2.40	77.62	0.24	0.00	11.02	0.00	0.07	0.12	0.31
	10 s	1.33	2.43	76.30	0.28	0.00	11.22	0.00	0.05	0.12	1.33
	5 s	0.00	2.18	77.44	0.25	0.00	11.62	0.00	0.06	0.13	0.00
	Ref [55]	0.07	2.11	72.28	0.12	0.06	11.83	0.08	0.05	0.06	0.07
SRM612	360 s	0.35	2.14	78.46	0.12	0.00	12.20	0.00	0.01	0.00	0.35
	180 s	0.34	2.16	78.50	0.12	0.00	12.16	0.00	0.01	0.00	0.34
	120 s	0.39	2.10	78.24	0.11	0.00	12.36	0.00	0.01	0.00	0.39
	60 s	0.00	2.10	78.60	0.12	0.00	12.41	0.00	0.01	0.00	0.00
	30 s	0.00	2.06	78.48	0.12	0.00	12.52	0.00	0.02	0.00	0.00
	20 s	0.30	2.12	78.30	0.15	0.00	12.31	0.00	0.01	0.00	0.30
	15 s	0.00	2.17	78.33	0.15	0.00	12.49	0.00	0.01	0.00	0.00
	10 s	0.59	2.03	78.16	0.09	0.00	12.29	0.00	0.01	0.00	0.59
	5 s	0.00	1.95	78.45	0.12	0.00	12.54	0.00	0.01	0.00	0.00
	Ref [55]	0.00	2.10	71.79	0.01	0.01	11.91	0.01	0.01	0.02	0.00
Corning A	360 s	4.77	1.14	72.00	0.21	2.96	5.27	1.01	0.99	1.26	4.77
	180 s	4.99	1.20	71.67	0.20	2.83	5.03	0.99	1.01	1.27	4.99
	120 s	4.87	1.25	71.78	0.21	2.83	5.03	0.99	1.02	1.27	4.87
	60 s	4.50	1.12	71.81	0.18	2.94	5.28	1.08	1.05	1.28	4.50
	30 s	4.67	1.22	71.30	0.17	2.93	5.25	1.10	1.09	1.36	4.67
	20 s	4.59	1.24	71.76	0.20	2.85	5.10	0.97	1.01	1.33	4.59
	15 s	4.48	1.25	71.96	0.20	2.85	5.15	0.99	1.03	1.27	4.48
	10 s	5.15	1.14	71.19	0.20	2.92	5.13	1.00	1.08	1.32	5.15
	5 s	5.86	1.21	70.88	0.21	2.78	4.96	1.04	1.05	1.22	5.86
	Ref [56]	2.66	1.00	66.56	0.08	2.87	5.03	0.79	1.00	1.09	2.66

Table A2. XRF data (wt%) showing the measurements #1 to #10 carried out on the body of IZN/15, IZN/16, IZN/17, and IZN/19.

Label	Spot	MgO	Al_2O_3	SiO_2	K_2O	CaO	Fe_2O_3	Rb_2O	SrO	ZrO_2	PbO
IZN/15	#1	2.11	5.19	80.21	1.16	2.22	1.28	0.00	0.01	0.00	0.63
	#2	1.45	4.62	81.53	0.97	2.12	1.27	0.00	0.01	0.01	0.88
	#3	2.03	4.78	78.80	1.07	2.68	1.44	0.00	0.01	0.01	0.89
	#4	2.35	5.93	74.90	1.35	3.30	2.07	0.00	0.01	0.01	1.23
	#5	1.88	5.17	80.26	1.22	2.19	1.40	0.00	0.01	0.00	0.70
	#6	2.14	5.90	78.08	1.26	2.64	1.64	0.00	0.01	0.01	0.95
	#7	2.02	5.33	77.49	1.17	2.77	1.81	0.01	0.01	0.01	1.12
	#8	2.13	5.63	76.31	1.19	3.08	1.66	0.00	0.01	0.01	1.20
	#9	2.40	5.69	76.21	1.12	3.02	1.30	0.00	0.01	0.01	1.58
	#10	1.85	4.73	80.78	1.03	2.17	1.34	0.00	0.01	0.01	0.87
IZN/16	#1	2.97	4.67	75.23	1.06	5.64	1.20	0.01	0.02	0.01	1.85
	#2	3.00	5.19	75.16	1.13	5.83	1.23	0.00	0.02	0.01	1.23
	#3	2.38	3.54	77.18	1.04	6.00	1.19	0.01	0.02	0.01	1.39
	#4	2.84	4.85	74.86	1.14	5.27	1.35	0.01	0.02	0.01	2.15
	#5	2.43	4.67	72.90	1.18	7.83	1.46	0.01	0.02	0.01	2.07
	#6	2.81	4.59	73.33	1.06	7.43	1.20	0.01	0.02	0.01	1.99
	#7	2.81	4.77	76.81	1.20	4.61	1.31	0.00	0.01	0.01	1.24
	#8	2.76	3.84	77.76	0.99	4.68	1.15	0.00	0.02	0.01	1.46
	#9	1.66	3.51	77.04	0.99	6.37	1.23	0.01	0.02	0.01	1.71
	#10	2.04	3.63	77.44	1.01	5.17	1.30	0.00	0.02	0.01	1.82
IZN/17	#1	2.29	5.18	76.00	1.08	3.92	1.52	0.01	0.01	0.01	1.40
	#2	2.73	5.21	72.81	1.12	3.99	1.51	0.01	0.01	0.01	1.54
	#3	2.25	6.68	72.27	1.43	3.92	1.81	0.01	0.01	0.01	1.56
	#4	2.29	5.59	72.37	1.17	4.11	1.77	0.01	0.01	0.01	1.92
	#5	2.49	7.09	72.08	1.57	3.71	2.04	0.01	0.01	0.01	1.69
	#6	2.20	5.37	78.13	1.18	2.75	1.43	0.00	0.01	0.01	1.23
	#7	2.14	5.19	74.34	1.11	4.41	1.63	0.00	0.01	0.01	1.44
	#8	1.72	5.11	78.62	1.05	2.46	1.47	0.01	0.01	0.01	1.29
	#9	2.19	5.48	74.60	1.16	4.29	1.58	0.01	0.01	0.01	1.46
	#10	2.44	6.04	72.80	1.31	4.03	1.73	0.01	0.01	0.01	1.84
IZN/19	#1	2.83	6.48	73.10	1.44	5.49	1.94	0.01	0.02	0.01	1.04
	#2	3.02	5.88	73.67	1.31	6.04	1.83	0.00	0.02	0.01	0.95
	#3	2.78	4.32	76.89	1.07	5.26	1.62	0.00	0.02	0.01	1.02
	#4	2.62	5.34	76.04	1.19	4.84	1.67	0.00	0.02	0.01	0.95
	#5	2.69	5.45	76.34	1.19	4.43	1.57	0.00	0.02	0.01	1.25
	#6	2.55	5.31	76.69	1.18	4.22	1.58	0.00	0.02	0.01	1.26
	#7	3.01	5.22	76.38	1.23	4.56	1.81	0.00	0.02	0.01	0.78
	#8	3.25	4.74	76.44	1.10	4.97	1.54	0.00	0.02	0.01	0.83
	#9	2.94	4.33	77.87	1.14	3.91	1.80	0.00	0.02	0.01	0.94
	#10	2.56	5.89	73.36	1.41	5.23	2.10	0.01	0.02	0.01	2.20

Table A3. XRF data (wt%) showing the measurements #1 to #10 carried out on the glaze of IZN/15, IZN/16, IZN/17, and IZN/19.

Label	Spot	MgO	Al_2O_3	SiO_2	K_2O	CaO	TiO_2	SnO_2	PbO
IZN/15	#1	1.29	1.06	51.77	0.68	1.47	0.25	0.32	37.75
	#2	1.45	1.40	52.76	0.76	1.36	0.22	0.34	36.54
	#3	0.91	1.12	50.84	0.70	1.39	0.26	0.37	39.26
	#4	1.32	1.82	55.91	0.98	2.32	0.26	0.26	31.20
	#5	1.09	1.98	55.66	1.12	2.61	0.79	0.28	30.20
	#6	1.75	1.30	50.15	0.77	1.47	0.29	0.36	38.63
	#7	1.21	1.25	51.39	0.76	1.48	0.25	0.33	37.99
	#8	1.31	1.31	51.60	0.78	1.47	0.26	0.35	37.64
	#9	0.64	1.17	52.46	0.70	1.41	0.24	0.36	37.80
	#10	1.70	1.37	52.04	0.75	1.37	0.23	0.29	37.05
IZN/16	#1	0.34	0.78	61.53	1.06	0.98	0.14	3.05	26.50
	#2	0.52	0.59	61.45	1.02	0.94	0.14	3.02	26.66
	#3	0.28	0.70	61.32	1.20	1.11	0.19	3.07	26.46
	#4	0.75	0.80	61.34	1.24	1.03	0.17	3.00	25.98
	#5	0.85	0.48	60.66	1.02	0.93	0.17	3.08	27.14
	#6	0.86	0.76	58.73	1.66	1.27	0.24	3.26	27.43
	#7	0.00	0.52	59.25	1.17	1.04	0.18	3.26	28.99
	#8	0.74	0.64	60.88	1.06	1.18	0.17	2.97	26.63
	#9	0.91	0.62	60.22	1.11	1.00	0.19	3.05	27.20
	#10	0.86	0.73	60.64	1.04	0.96	0.15	3.03	26.97
IZN/17	#1	1.26	1.45	49.41	0.88	2.03	0.31	0.48	38.33
	#2	1.33	3.50	57.36	1.52	1.20	0.13	0.34	29.17
	#3	1.21	1.45	51.23	0.88	1.49	0.24	0.50	37.58
	#4	1.18	1.85	50.76	1.00	1.85	0.30	0.50	36.46
	#5	0.86	3.44	57.28	1.52	1.16	0.14	0.36	29.85
	#6	1.43	1.61	50.69	0.90	1.24	0.23	0.47	38.14
	#7	1.30	3.38	57.00	1.48	1.19	0.20	0.37	29.62
	#8	1.38	1.45	51.15	0.83	1.30	0.29	0.49	37.85
	#9	1.33	1.28	50.74	0.79	1.23	0.28	0.51	38.54
	#10	1.56	1.58	48.61	0.94	1.69	0.34	0.50	38.96
IZN/19	#1	0.99	0.96	36.42	0.80	2.64	0.50	0.33	50.19
	#2	1.74	2.13	52.75	0.92	3.41	0.66	0.18	30.64
	#3	2.63	1.60	39.96	0.83	3.18	0.67	0.28	43.07
	#4	1.50	1.17	39.53	0.67	2.66	0.43	0.29	46.07
	#5	1.65	1.20	37.89	0.84	3.06	3.52	0.28	43.88
	#6	2.40	1.01	32.23	0.70	4.19	0.63	0.34	48.45
	#7	1.61	1.12	31.91	0.71	4.38	0.63	0.32	48.70
	#8	1.32	1.13	33.93	0.70	3.83	0.66	0.33	48.74
	#9	2.80	1.22	32.65	0.69	4.23	0.70	0.31	47.29
	#10	1.61	1.22	37.67	0.76	3.92	0.60	0.30	44.69

Table A4. XRF data (wt%) showing the measurements #1 to #10 carried out on the blue coloured areas of IZN/15, IZN/16, IZN/17, and IZN/19.

Label	Spot	SiO_2	TiO_2	V_2O_5	Cr_2O_3	MnO	Fe_2O_3	CoO	NiO	CuO	ZnO	SnO_2	PbO	Bi_2O_3
IZN/15	#1	51.23	0.21	0.49	0.07	0.02	0.35	0.04	0.02	0.19	0.01	0.36	38.62	0.10
	#2	49.40	0.32	0.54	0.05	0.03	0.36	0.07	0.03	0.19	0.01	0.35	39.61	0.11
	#3	50.65	0.24	0.51	0.07	0.03	0.36	0.05	0.02	0.18	0.01	0.36	39.11	0.13
	#4	50.05	0.27	0.51	0.06	0.00	0.36	0.05	0.03	0.30	0.01	0.35	39.26	0.11
	#5	51.21	0.26	0.48	0.07	0.03	0.46	0.07	0.03	0.18	0.01	0.31	37.82	0.13
	#6	50.60	0.27	0.49	0.07	0.01	0.39	0.08	0.04	0.11	0.01	0.35	38.07	0.14
	#7	51.23	0.22	0.50	0.06	0.03	0.36	0.04	0.02	0.24	0.01	0.36	38.45	0.10
	#8	50.20	0.25	0.51	0.07	0.02	0.37	0.02	0.01	0.71	0.01	0.38	38.89	0.09
	#9	49.91	0.25	0.52	0.05	0.01	0.36	0.03	0.02	0.19	0.01	0.36	39.47	0.10
	#10	50.41	0.26	0.51	0.07	0.02	0.36	0.04	0.02	0.53	0.01	0.35	38.66	0.09
IZN/16	#1	59.82	0.21	0.38	0.06	0.03	0.44	0.05	0.02	0.47	0.01	3.04	27.13	0.11
	#2	60.15	0.22	0.37	0.07	0.02	0.43	0.06	0.02	0.43	0.01	3.00	26.96	0.14
	#3	57.37	0.30	0.00	0.05	0.02	0.49	0.04	0.01	0.38	0.01	3.33	28.45	0.14
	#4	61.16	0.19	0.36	0.09	0.02	0.41	0.04	0.01	0.43	0.01	3.04	26.88	0.11
	#5	60.94	0.15	0.00	0.05	0.03	0.44	0.03	0.01	0.44	0.01	2.99	26.77	0.10
	#6	59.94	0.19	0.37	0.00	0.04	0.40	0.05	0.02	0.48	0.01	3.15	27.72	0.12
	#7	60.82	0.16	0.36	0.06	0.03	0.40	0.04	0.01	0.44	0.01	3.03	27.19	0.11
	#8	61.41	0.14	0.00	0.07	0.03	0.41	0.04	0.02	0.47	0.01	3.03	27.02	0.11
	#9	60.49	0.17	0.00	0.07	0.03	0.42	0.04	0.01	0.44	0.01	3.03	26.77	0.14
	#10	60.47	0.16	0.00	0.07	0.02	0.43	0.05	0.01	0.47	0.01	3.05	27.08	0.12
IZN/17	#1	51.69	0.27	0.51	0.06	0.05	0.41	0.07	0.02	0.17	0.02	0.49	37.28	0.12
	#2	47.84	0.32	0.49	0.08	0.05	0.45	0.08	0.02	0.28	0.02	0.51	39.15	0.12
	#3	50.26	0.29	0.48	0.07	0.05	0.43	0.05	0.01	0.14	0.02	0.47	37.06	0.14
	#4	50.66	0.24	0.51	0.06	0.05	0.42	0.06	0.02	0.16	0.01	0.49	37.88	0.12
	#5	56.05	0.13	0.00	0.06	0.05	0.38	0.08	0.02	0.12	0.02	0.37	29.80	0.10
	#6	51.10	0.22	0.48	0.07	0.05	0.42	0.07	0.02	0.21	0.02	0.48	37.35	0.14
	#7	51.01	0.23	0.47	0.06	0.04	0.44	0.06	0.02	0.26	0.02	0.47	36.99	0.12
	#8	48.38	0.30	0.53	0.05	0.05	0.47	0.07	0.02	0.20	0.02	0.52	40.67	0.14
	#9	49.57	0.30	0.48	0.05	0.07	0.44	0.08	0.02	0.28	0.02	0.52	38.48	0.14
	#10	51.87	0.26	0.48	0.05	0.04	0.42	0.08	0.02	0.16	0.02	0.46	35.92	0.14
IZN/19	#1	31.90	0.80	0.53	0.12	0.05	0.59	0.03	0.02	0.58	0.02	0.34	52.94	0.10
	#2	39.24	0.55	0.52	0.19	0.06	0.76	0.04	0.03	0.51	0.02	0.28	45.99	0.09
	#3	39.47	1.71	0.45	0.06	0.05	0.61	0.03	0.03	0.43	0.02	0.26	42.60	0.08
	#4	38.20	0.56	0.54	0.23	0.03	0.85	0.02	0.02	0.43	0.02	0.27	44.01	0.10
	#5	39.06	0.44	0.51	0.08	0.07	0.48	0.05	0.04	0.46	0.02	0.29	46.06	0.08
	#6	37.87	0.49	0.49	0.08	0.05	0.60	0.04	0.03	0.50	0.02	0.30	48.44	0.08
	#7	39.90	0.50	0.53	0.23	0.04	0.86	0.03	0.02	0.44	0.02	0.27	44.78	0.10
	#8	36.78	0.52	0.53	0.00	0.05	0.58	0.04	0.03	0.44	0.02	0.30	46.77	0.09
	#9	31.46	0.60	0.57	0.00	0.05	0.52	0.02	0.02	0.43	0.02	0.35	47.89	0.10
	#10	33.11	0.59	0.55	0.05	0.04	0.50	0.05	0.03	0.41	0.02	0.31	46.63	0.07

References

1. Craig, N.; Speakman, R.J.; Popelka-Filcoff, R.S.; Aldenderfer, M.; Blanco, L.F.; Vega, M.B.; Glascock, M.D.; Stanish, C. Macusani obsidian from southern Peru: A characterization of its elemental composition with a demonstration of its ancient use. *J. Archaeol. Sci.* **2010**, *37*, 569–576. [CrossRef]
2. Frahm, E.; Goldstein, S.T.; Tryon, C.A. Late Holocene forager-fisher and pastoralist interactions along the Lake Victoria shores, Kenya: Perspectives from portable XRF of obsidian artifacts. *J. Archaeol. Sci. Rep.* **2017**, *11*, 717–742. [CrossRef]
3. Liu, S.; Li, Q.H.; Fu, Q.; Gan, F.X.; Xiong, Z.M. Application of a portable XRF spectrometer for classification of potash glass beads unearthed from tombs of Han Dynasty in Guangxi, China. *X-ray Spectrom.* **2013**, *42*, 470–479. [CrossRef]

4. Fermo, P.; Andreoli, M.; Bonizzoni, L.; Fantauzzi, M.; Giubertoni, G.; Ludwig, N.; Rossi, A. Characterisation of Roman and Byzantine glasses from the surroundings of Thugga (Tunisia): Raw materials and colours. *Microchem. J.* **2016**, *129*, 5–15. [CrossRef]
5. Licenziati, F.; Calligaro, T. Study of mosaic glass tesserae from Delos, Greece using a combination of portable μ-Raman and X-ray fluorescence spectrometry. *J. Archaeol. Sci. Rep.* **2016**, *7*, 640–648. [CrossRef]
6. Zhao, H.X.; Li, Q.H. Combined spectroscopic analysis of stratified glass eye beads from China dated to the Warring States Period. *J. Raman Spectrosc.* **2017**, *48*, 1103–1110. [CrossRef]
7. Forster, N.; Grave, P. Effects of elevated levels of lead in ceramics on provenancing studies using non-destructive PXRF: A case study in Byzantine Cypriot glazed ceramics. *X-ray Spectrom.* **2013**, *42*, 480–486. [CrossRef]
8. Xu, W.; Niziolek, L.C.; Feinman, G.M. Sourcing qingbai porcelains from the Java Sea Shipwreck: Compositional analysis using portable XRF. *J. Archaeol. Sci.* **2019**, *103*, 57–71. [CrossRef]
9. Frankel, D.; Webb, J.M. Pottery production and distribution in prehistoric Bronze Age Cyprus. An application of pXRF analysis. *J. Archaeol. Sci.* **2012**, *39*, 1380–1387. [CrossRef]
10. Padilla, J.T.; Hormes, J.; Selim, H.M. Use of portable XRF: Effect of thickness and antecedent moisture of soils on measured concentration of trace elements. *Geoderma* **2019**, *337*, 143–149. [CrossRef]
11. Hunt, A.M.W.; Speakman, R.J. Portable XRF analysis of archaeological sediments and ceramics. *J. Archaeol. Sci.* **2015**, *53*, 626–638. [CrossRef]
12. Laskaris, N.; Varalis, I.; Tsodoulos, C.; Dolmas, C. Evidence of Au-Hg gilding process in post Byzantine ecclesiastical silverwares (chalices) of eastern Thessaly by pXRF. *Mediterranean* **2020**, *20*, 189–203.
13. Roxburgh, M.A.; Heeren, S.; Huisman, D.J.; Van Os, B.J.H. Non-Destructive Survey of Early Roman Copper-Alloy Brooches using Portable X-ray Fluorescence Spectrometry. *Archaeometry* **2018**, *61*, 55–69. [CrossRef]
14. Ganetsos, T.; Regkli, A.; Laskaris, N.; Liritzis, I. Spectroscopic study of colour traces in marble sculptures and architectural parts of monuments of archaic period in Delphi, Greece. *Mediterranean* **2019**, *19*, 51–61.
15. Garrido, F.; Li, T. A handheld XRF study of Late Horizon metal artifacts: Implications for technological choices and political intervention in Copiap, northern Chile. *Archaeol. Anthrop. Sci.* **2017**, *9*, 935–942. [CrossRef]
16. Brand, N.W.; Brand, C.J. Performance comparison of portable XRF instruments. *Geochem. Explor. Environ. Anal.* **2014**, *14*, 125–138. [CrossRef]
17. Frahm, E. Validity of "off-the-shelf" handheld portable XRF for sourcing Near Eastern obsidian chip debris. *J. Archaeol. Sci.* **2013**, *40*, 1080–1092. [CrossRef]
18. Goodale, N.; Bailey, D.G.; Jones, G.T.; Prescott, C.; Scholz, E.; Stagliano, N.; Lewis, C. pXRF: A study of inter-instrument performance. *J. Archaeol. Sci.* **2012**, *39*, 875–883. [CrossRef]
19. Liritzis, I.; Zacharias, N. Portable XRF of Archaeological Artifacts: Current Research, Potentials and Limitations. In *X-ray Fluorescence Spectrometry (XRF) in Geoarchaeology*, 1st ed.; Schackley, M.S., Ed.; Springer: New York, NY, USA, 2011; pp. 109–142.
20. Shackley, M.S. Is there reliability and validity in portable X-ray fluorescence spectrometry (PXRF)? *SAA Archaeol. Rec.* **2010**, *10*, 17–20.
21. Speakman, R.J.; Shackley, M.S. Silo science and portable XRF in archaeology: A response to Frahm. *J. Archaeol. Sci.* **2013**, *40*, 1435–1443. [CrossRef]
22. Stroth, L.; Otto, R.; Daniels, J.T.; Braswell, G.A. Statistical artifacts: Critical approaches to the analysis of obsidian artifacts by portable X-ray fluorescence. *J. Archaeol. Sci. Rep.* **2019**, *24*, 738–747. [CrossRef]
23. NIST X-ray Mass Attenuation Coefficients. Available online: https://www.nist.gov/pml/x-ray-mass-attenuation-coefficients (accessed on 12 September 2020).
24. Koleini, F.; Colomban, P.; Pikirayi, I. Post-15th century European glass beads in southern Africa: Composition and classification using pXRF and Raman spectroscopy. *J. Archaeol. Sci. Rep.* **2020**, *29*, 102183. [CrossRef]
25. Bonizzoni, L.; Galli, A.; Gondola, M.; Martini, M. Comparison between XRF, TXRF, and PXRF analyses for provenance classification of archaeological bricks. *X-ray Spectrom.* **2013**, *42*, 262–267. [CrossRef]
26. Mitchell, D.; Grave, P.; Maccheroni, M.; Gelman, E. Geochemical characterisation of north Asian glazed stonewares: A comparative analysis of NAA, ICP-OES and non-destructive pXRF. *J. Archaeol. Sci.* **2012**, *39*, 2921–2933. [CrossRef]
27. Adlington, L.; Gratuze, B.; Schibille, N. Comparison of pXRF and LA-ICP-MS analysis of lead-rich glass mosaic tesserae. *J. Archaeol. Sci. Rep.* **2020**, *34*, 102603. [CrossRef]

28. Aydemir, D.; Karabulut, G.; Şimşek, G.; Gok, M.; Barlas, N.; Ulusu, N.N. Impact of the Di(2-Ethylhexyl) Phthalate Administration on Trace Element and Mineral Levels in Relation of Kidney and Liver Damage in Rats. *Biol. Trace Element Res.* **2018**, *186*, 474–488. [CrossRef]
29. Franci, G.S. Handheld X-ray fluorescence (XRF) versus wavelength dispersive XRF: Characterization of Chinese blue-and-white porcelain sherds using handheld and laboratoy-type XRF instruments. *Appl. Spectrosc.* **2020**, *74*, 314–322. [CrossRef]
30. Franci, G.S.; Akkas, T.; Yildirim, S.; Yilmaz, S.; Birdevrim, A.N. Characterization of a Jian-like sherd with the optical microscope, confocal Raman, wavelength-dispersive X-ray fluorescence, and portable XRF spectrometers. *J. Raman Spectrosc.* **2020**, *51*, 1343–1352. [CrossRef]
31. Simsek, G.; Colomban, P.; Casadio, F.; Bellot-Gurlet, L.; Zelleke, G.; Faber, K.T.; Milande, V.; Tilliard, L. On-Site Identification of Early Böttger Red Stoneware Using Portable XRF/Raman Instruments: 2, Glaze & Gilding Analysis. *J. Am. Ceram. Soc.* **2015**, *98*, 3006–3013. [CrossRef]
32. Simsek, G.; Arli, B.D.; Kaya, S.; Colomban, P. On-site pXRF analysis of body, glaze and colouring agents of the tiles at the excavation site of Iznik kilns. *J. Eur. Ceram. Soc.* **2019**, *39*, 2199–2209. [CrossRef]
33. Simsek, G.; Unsalan, O.; Bayraktar, K.; Colomban, P. On-site pXRF analysis of glaze composition and colouring agents of « Iznik » tiles at Edirne mosques (15th and 16th-centuries). *Ceram. Int.* **2019**, *45*, 595–605. [CrossRef]
34. Demirsar Arli, V.B.; Kaya, S.; Simsek Franci, G. Assessment of impressed/moulded ceramic wares excavated during the 2018–2019 seasons at the Iznik Tile Kilns Excavation and analysis results with a pXRF instrument on selected samples. *Sanat Tarihi Yilligi* **2020**, *29*, 1–19.
35. Atasoy, N.; Raby, J. *Iznik: The Pottery of Ottoman Turkey*, 1st ed.; Alexandria Press: London, UK, 1989; pp. 1–384.
36. Carswell, J. *Iznik Pottery (Eastern Art)*, 1st ed.; British Museum Press: London, UK, 1998; pp. 1–128.
37. Denny, W.B. *Iznik La Céramique Turque et l'Art Ottoman*, 1st ed.; Citadelles and Mazenod: Paris, France, 2004; pp. 1–239.
38. Soustiel, J. *La Céramique Islamique—Le Guide du Connaisseur, Office du Livre*, 1st ed.; Editions Vilo: Paris, France, 1985.
39. Valenstein, S.G. *A Handbook of Chinese Ceramics*, 2nd ed.; Metropolitan Museum of Art: New York, NY, USA, 1989; pp. 1–331.
40. Trubner, H. *Ceramic Art of Japan: One Hundred Masterpieces from Japanese Collections*, 1st ed.; Seattle Art Museum: Reno, NV, USA, 1973; pp. 1–172.
41. Penkala, M. *European Porcelain; A Handbook for the Collector*, 2nd ed.; C.E. Tuttle Co.: Rutland, VT, USA, 1968; pp. 1–256.
42. Migeon, G.; Sakisian, A. *La céramique d'Asie-Mineure et de Constantinople du XIVe au XVIIIe siècle*, 1st ed.; Extrait de La Revue de l'Art Ancien et Moderne, Tomes XLIII-XLIV, Librairie Orientaliste Paul Geuthner: Paris, France, 1923; pp. 1–46.
43. Koechlin, R.; Migeon, G. 100 planches en couleurs d'Art musulman (céramique, tissus, tapis). *Syr. Archéologie Art Hist.* **1929**, *10*, 173–174.
44. Lane, A. The Ottoman pottery of Isnik. *Ars Orient.* **1957**, *2*, 247–281.
45. Riefstahl, R.M. Early Turkish tile-revetments in Edirne. *Ars Islam.* **1937**, *4*, 249–281.
46. Kiefer, C. Les céramiques musulmanes d'Anatolie. *Cah. Céram. Arts Feu.* **1956**, *4*, 15–30.
47. Kiefer, C. Les céramiques siliceuses d'Anatolie et du Moyen-Orient. *Bull. Soc. Fr. Céram.* **1956**, *30*, 3–24, reprinted in **1956**, *31*, 17–34.
48. Rackham, B. Turkish pottery. *Trans. Orient. Ceram. Soc.* **1934**, *12*, 35–48.
49. Henderson, J.; Raby, J. The technology of fifteenth century Turkish tiles: An interim statement on the origins of the Iznik industry. *World Archaeol.* **1989**, *21*, 115–132. [CrossRef]
50. Arli, B.D.; Altun, A. *Anadolu Toprağının Hazinesi Çini, Osmanlı Dönemi*, 1st ed.; Kale Grubu Kültür Yayınları: İstanbul, Turkey, 2008; pp. 1–373.

51. Arli, B.D.; Adıgüzel, H. The Connection Between the Tile Decoration of the 16th and 17th Centuries in Istanbul with the Tile Fragments Found in Iznik Excavations. In *The Art of the Islamic World and the Artistic Relationships between Polland and Islamic Countries, Proceedings of 11th Conference of the Polish Institute of World Art Studies (Former Polish Society of Oriental Art), 1st Conference of Islamic Art in Poland, Krakow, Poland, 5–7 October 2009*; Slota, B.B., Ginter-Frolow, M., Malinowski, J., Eds.; Manggha, Polish Institute of World Art Studies: Krakow, Poland, 2011; pp. 235–245.
52. Arlı, B.D. İznik Çini Fırınları Kazı Buluntularından Çini Örneklerin Değerlendirilmesi/Evaluation of Iznik Tiles Examples from Iznik Tile Excavation. *J. Hist. Cult. Art Res.* **2018**, *7*, 578–594. [CrossRef]
53. Özer, M.; Dündar, M.; Güner, Y.; Uçar, H. Edirne Yeni Saray Kazısı (Saray-ı Cedîd-i Âmire) 2011 Yılı Çalışmaları. *Sanat Tarihi Derg.* **2016**, *24*, 73–106. [CrossRef]
54. Arlı, B.D.; Kaya, S. İznik Çini Fırınları Kazısı Çini Buluntularının Değerlendirilmesi. In Proceedings of the 16th International Congress of Turkish Art (ICTA), Ankara, Turkey, 3–5 October 2015.
55. Adlington, L.W. The Corning Archaeological Reference Glasses: New Values for "Old" Compositions. *Pap. Inst. Archaeol.* **2017**, *27*, 1–8. [CrossRef]
56. Pearce, N.J.; Perkins, W.T.; Westgate, J.A.; Gorton, M.P.; Jackson, S.E.; Neal, C.R.; Chenery, S.P. A Compilation of New and Published Major and Trace Element Data for NIST SRM 610 and NIST SRM 612 Glass Reference Materials. *Geostand. Geoanalytical Res.* **1997**, *21*, 115–144. [CrossRef]
57. Conrey, R.M.; Goodman-Elgar, M.; Bettencourt, N.; Seyfarth, A.; Van Hoose, A.; Wolff, J.A. Calibration of a portable X-ray fluorescence spectrometer in the analysis of archaeological samples using influence coefficients. *Geochem. Explor. Environ. Anal.* **2014**, *14*, 291–301. [CrossRef]
58. Tournie, A.; Ricciardi, P.; Colomban, P. Glass corrosion mechanisms: A multiscale analysis. *Solid State Ion.* **2008**, *179*, 2142–2154. [CrossRef]
59. Pradell, T.; Molera, J. Ceramic technology. How to characterise ceramic glazes. *Archaeol. Anthr. Sci.* **2020**, *12*, 1–28. [CrossRef]
60. Paynter, S.; Okyar, F.; Wolf, S.; Tite, M.S. The production technology of Iznik pottery—A reassessment. *Archaeometry* **2004**, *46*, 421–437. [CrossRef]
61. Colomban, P.; Kırmızı, B.; Gougeon, C.; Gironda, M.; Cardinal, C. Pigments and glassy matrix of the 17th–18th century enamelled French watches: A non-invasive on-site Raman and pXRF study. *J. Cult. Herit.* **2020**, *44*, 1–14. [CrossRef]
62. Tite, M. Iznik pottery: An investigation of the methods of production. *Archaeometry* **1989**, *31*, 115–132. [CrossRef]
63. Matin, M. Tin-based opacifiers in archaeological glass and ceramic glazes: A review and new perspectives. *Archaeol. Anthr. Sci.* **2018**, *11*, 1155–1167. [CrossRef]
64. Vane-Tempest, S.; Kronberg, T.; Fröberg, L.; Hupa, L. Chemical Resistance of Fast-Fired Raw Glazes in Solutions Containing Cleaning Agent, Acids or Bases. Qualicer 2004. Available online: http://www.qualicer.org/recopilatorio/ponencias/pdfs/0413121e.pdf (accessed on 29 September 2020).
65. Colomban, P. Rocks as blue, green and black pigments/dyes of glazed pottery and enamelled glass artefacts? A review. *Eur. J. Miner.* **2014**, *25*, 863–879. [CrossRef]
66. Colomban, P. Routes du lapis lazuli, lajvardina et échanges entre arts du verre, de la céramique et du livre. *Taıci* **2005**, *4*, 145–152.
67. Kissin, S.A. Five element (Ni-Co-As-Ag-Bi) veins. *Geosci. Can.* **1992**, *19*, 113–124.
68. Wen, R.; Pollard, A.M. The Pigments Applied to Islamic Minai Wares and the Correlation with Chinese Blue-and-White Porcelain. *Archaeometry* **2014**, *58*, 1–16. [CrossRef]
69. Colomban, P.; Sagon, G.; Huy, L.Q.; Liem, N.Q.; Mazerolles, L. Vietnamese (15th Century) Blue-And-White, Tam Thai and Lustre Porcelains/Stonewares: Glaze Composition and Decoration Techniques. *Archaeometry* **2004**, *46*, 125–136. [CrossRef]
70. Simsek, G.; Colomban, P.; Wong, S.; Zhao, B.; Rougeulle, A.; Liem, N.Q. Toward a fast non-destructive identification of pottery: The sourcing of 14th–16th century Vietnamese and Chinese ceramic shards. *J. Cult. Herit.* **2015**, *16*, 159–172. [CrossRef]
71. Fischer, C.; Hsieh, E. Export Chinese blue-and-white porcelain: Compositional analysis and sourcing using non-invasive portable XRF and reflectance spectroscopy. *J. Archaeol. Sci.* **2017**, *80*, 14–26. [CrossRef]
72. Du, F.; Su, B. Further study of sources of the imported cobalt-blue pigment used on Jingdezhen porcelain from late 13 to early 15 centuries. *Sci. China Ser. E Technol. Sci.* **2008**, *51*, 249–259. [CrossRef]

73. Figueiredo, M.; Silva, T.P.; Veiga, J.P. A XANES study of cobalt speciation state in blue-and-white glazes from 16th to 17th century Chinese porcelains. *J. Electron Spectrosc.* **2012**, *185*, 97–102. [CrossRef]
74. Zhu, T.Q.; Zhang, Y.C.; Xiong, H.; Feng, Z.Y.; Li, Q.; Cao, B.L. Comparison of the different types of Qinghua porcelain from Jingdezhen in the Yuan Dynasty of China (AD 1271–1368) by micro X-ray fluorescence spectroscopy (μ-XRF) and microscopy. *Archaeometry* **2016**, *58*, 966–978. [CrossRef]
75. Pappalardo, G.; Costa, E.; Marchetta, C.; Pappalardo, L.; Romano, F.P.; Zucchiatti, A.; Prati, P.; Mando, P.A.; Migliori, A.; Palombo, L.; et al. Non-destructive characterization of Della Robia sculptures at the Bargello museum in Florence by the combined use of PIXE and XRF portable systems. *J. Cult. Herit.* **2004**, *5*, 183–188. [CrossRef]
76. Zucchiatti, A.; Bouquillon, A.; Katona, I.; D'Alessandro, A. The 'Della Robia Blue': A case study for the use of cobalt pigments in ceramics during the Italian renaissance. *Archaeometry* **2006**, *48*, 131–152. [CrossRef]
77. Barilaro, D.; Crupi, V.; Interdonato, S.; Majolino, D.; Venuti, V.; Barone, G.; La Russa, M.F.; Bardelli, F. Characterization of blue decorated Renaissance pottery fragments from Caltagirone (Siciliy, Italy). *Appl. Phys. A* **2008**, *92*, 91–96. [CrossRef]
78. Porter, Y. Le cobalt dans le monde iranien (IXe-XVIe siecles): Notes sur son utilization en céramique et son commerce. *Taoci* **2000**, *1*, 5–14.
79. Matin, M.; Pollard, A.M. Historical Accounts of Cobalt Ore Processing from the Kashan Mine, Iran. *Iran* **2015**, *53*, 171–183. [CrossRef]